

Proxies for Distortion and Consistency with Applications for Real-World Image Restoration

Sean Man Guy Ohayon Ron Raphaeli Michael Elad
Technion – Israel Institute of Technology

{sean.man, ohayonguy, ronraphaeli, elad}@cs.technion.ac.il

Abstract

Real-world image restoration deals with the recovery of images suffering from an unknown degradation. This task is typically addressed while being given only degraded images, without their corresponding ground-truth versions. In this hard setting, designing and evaluating restoration algorithms becomes highly challenging. This paper offers a suite of tools that can serve both the design and assessment of real-world image restoration algorithms. Our work starts by proposing a trained model that predicts the chain of degradations a given real-world measured input has gone through. We show how this estimator can be used to approximate the consistency – the match between the measurements and any proposed recovered image. We also use this estimator as a guiding force for the design of a simple and highly-effective plug-and-play real-world image restoration algorithm, leveraging a pre-trained diffusion-based image prior. Furthermore, this work proposes no-reference proxy measures of MSE and LPIPS, which, without access to the ground-truth images, allow ranking of real-world image restoration algorithms according to their (approximate) MSE and LPIPS. The proposed suite provides a versatile, first of its kind framework for evaluating and comparing blind image restoration algorithms in real-world scenarios.

1. Introduction

Image restoration – the task of reconstructing high-quality images from their degraded measurements (e.g., noisy, blurry) – is one of the most extensively studied problems in imaging sciences. The typical foundation for designing and testing image restoration algorithms is the assumption that the degradation process (forward model) is known and follows a specific mathematical form. In image denoising, for example, the noise contamination is commonly assumed to be additive, white, and Gaussian with a known variance [7, 10, 12, 13, 15, 17, 27, 30, 44, 70, 71]. This enables synthesizing corresponding pairs of clean images

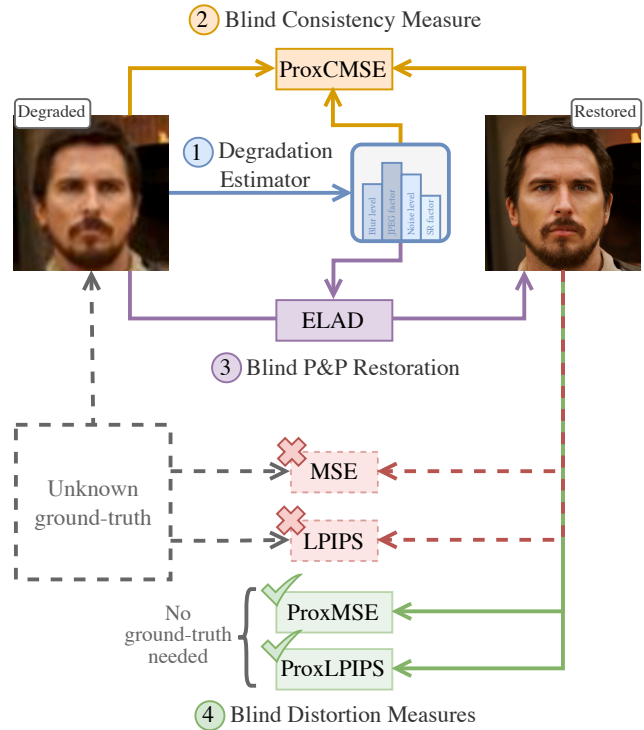


Figure 1. This work introduces several novel tools to help tackle the challenging task of real-world image restoration. We propose ① an estimator that predicts the degradations a real-world corrupted measurement has gone through. Using this estimator, we ② approximate the consistency of any reconstructed candidate with a given input measurement, and use such a measure to develop ③ a plug-and-play real-world restoration algorithm. Moreover, we propose ④ blind (no-reference) measures of distortion that mimic MSE and LPIPS, thus eliminating the need for ground-truth images when comparing the distortion of real-world image restoration algorithms.

and degraded measurements, which can then be used for supervised learning (e.g., minimizing the MSE [64]) and/or evaluation (e.g., computing distortion measures such as

PSNR, SSIM [65], and LPIPS [73]). The mathematical expression of the degradation process can also be leveraged to design plug-and-play image restoration algorithms [8, 27, 28, 40, 48, 59, 63, 76]. Indeed, the gradient of the log-likelihood function $\log p_{Y|X}(y|x)$ w.r.t. x , where X and Y are random vectors denoting the ground-truth image and the degraded measurement, respectively, is often used for guiding the sampling from the posterior distribution [8, 27, 28, 40, 63, 76].

As opposed to the above, the degradation process is typically unknown in real-world scenarios [23, 42, 62, 72], making it significantly more challenging to design and evaluate image restoration algorithms for everyday applications. This paper offers several focused contributions that aim to foster progress in such real-world scenarios, circumventing the above described difficulties. We start by introducing a highly-effective learnable model that predicts the chain of degradations a given real-world input has gone through (Figure 1). As we show, this estimator can then be leveraged in three important ways: (i) We rely on it for the development of a *blind* consistency measure – an approximation of the likelihood of any reconstructed candidate image given a real-world degraded input; (ii) Using this approximate-likelihood measure, we considerably improve the distortion and consistency of DiffFace [69], by guiding the generated images to remain consistent with the inputs in a plug-and-play manner; (iii) Finally, we use the degradation estimator for synthesizing pairs of clean images and their corresponding degraded measurements, in a way that mimics any existing dataset of real-world inputs.

Beyond all the above, we also propose *blind* proxy measures of MSE and LPIPS, as illustrated in Figure 1. With no access to the ground-truth images of the given real-world degraded inputs, these measures can be used to rank real-world image restoration algorithms according to their (approximate) MSE and LPIPS.

This paper is organized as follows: We begin with the problem’s formulation and notations in Section 2. Our degradation estimator and likelihood approximation approach are described in Section 3, along with their derivative applications. In Section 4 we introduce our blind (no-reference) proxy distortion measures, and use them to evaluate real-world restoration methods on blind face restoration datasets. We conclude with a discussion on related work in Section 5, and the limitations and possible future directions in Section 6.

2. Preliminaries

As in [3], we consider a natural image x to be a realization of a random vector X with probability density function p_X . A degraded measurement y is also a realization of a random vector Y , which is related to X via the conditional probability density function $p_{Y|X}$. Generally speaking, an image

restoration algorithm is some estimator \hat{X} that generates reconstructions according to $p_{\hat{X}|Y}$, where $X \rightarrow Y \rightarrow \hat{X}$ (X and \hat{X} are statistically independent given Y).

The degradation process is typically unknown in real-world scenarios. Namely, a given real-world measurement can result from many different variations over the possible degradation processes. We denote by A the random vector that represents all the possible degradation processes that y could have gone through, and by p_A its density. Thus, we can generally say that the degraded measurement y is sampled from the conditional density $p_{Y|X,A}(\cdot|x, a)$, where x and a are realizations of the random vectors X and A , respectively, which are sampled jointly and independently. In blind face image restoration (BFR), the degradation process is commonly modeled [16, 31, 61, 69, 75] as

$$Y = \text{JPEG}_Q((K * x) \downarrow_S + N), \quad (1)$$

where $A = (K, S, \sigma_N, Q)^\top$ is a random vector: K is a Gaussian blur kernel of width σ_K , \downarrow_S denotes the bilinear down-sampling operator with scale-factor S , $N \sim \mathcal{N}(0, \sigma_N^2 I)$ is a white Gaussian noise with standard deviation σ_N , and JPEG_Q is JPEG compression-decompression algorithm with quality-factor Q . Throughout the paper, we consider the BFR task for demonstrating our proposed tools, where σ_K, S, σ_N and Q in Eq. (1) are sampled independently and uniformly from $[0.1, 15]$, $[1, 32]$, $[0, 20/255]$, $[30, 100]$, respectively (as in DiffFace [69]), unless mentioned otherwise.

3. Empirical likelihood approximation (ELA)

The conditional probability density function $p_{Y|X}$ leads to the definition of the *log-likelihood function* $\ell(y, x) = \log p_{Y|X}(y|x)$, where a larger value of $\ell(y, x)$ implies that the image x is more *consistent* with the measurement y . Such a likelihood function has several practical benefits in image restoration. For instance, it facilitates plug-and-play image restoration, where the outputs generated by a pre-trained diffusion model are enforced to be consistent with the given measurement [8, 27, 28, 40, 48, 59, 63, 76]. However, $p_{Y|X}$ is typically unknown in real-world scenarios, so $\ell(y, x)$ cannot be used directly. To overcome such a limitation, we introduce *Empirical Likelihood Approximation* (ELA), an approach to approximate $\ell(y, x)$ based on a novel degradation estimator. Utilizing the proposed likelihood function, we present a blind consistency measure for real-world problems, followed by a plug-and-play restoration method for blind face restoration that harnesses a pre-trained diffusion prior.

3.1. Approximate log-likelihood

Many of the algorithms that operate in non-blind settings (where $p_{Y|X}$ is known) focus on deterministic degradation

operators with additive Gaussian noise. This leads to the familiar log-likelihood expression

$$\ell(y, x) \propto -\|y - h(x)\|_2^2, \quad (2)$$

where h is some deterministic degradation operator (e.g., bicubic down-sampling). Suppose that $Y = y$ is coupled with an appropriate $A = a$, namely y is the degraded measurement that resulted from the degradation corresponding to a . We approximate the log-likelihood function corresponding to such a degradation by

$$\ell(y, x) \approx -\|y - \mu_Y(x, a)\|_2^2, \quad (3)$$

where $\mu_Y(x, a) := \mathbb{E}[Y|X = x, A = a]$, and the expectation is taken w.r.t. the remaining stochastic portions of the degradation $A = a$ (such as noise). To design an appropriate log-likelihood function for an unknown degradation, we train a model to predict A from Y , and then use the result in Eq. (3). Namely,

$$\ell(y, x) \approx -\|y - \mu_Y(x, a_\theta(y))\|_2^2 \quad (4)$$

is our final approximation of the log-likelihood, where a_θ is a trained model which estimates A from Y .

3.2. Degradation estimator

Given a measurement y , the task of the estimator $a_\theta(y)$ is to predict the degradation that produced y , i.e. $a_\theta(y) \approx a$. For the task of blind face restoration, we train a regression model to estimate the degradation parameters described in Eq. (1). To train our model, we incorporate the standard squared error regression loss $\mathcal{L}_{\text{Main}} = \|a - a_\theta(y)\|_2^2$. Moreover, to ensure that the predicted solution aligns with $\mu_Y(x, a)$, we also add the regularization term $\mathcal{L}_{\text{Reg.}} = \|\mu_Y(x, a) - \mu_Y(x, a_\theta(y))\|_2^2$. Our final training loss is given by $0.25\mathcal{L}_{\text{Main}} + \mathcal{L}_{\text{Reg.}}$. Figure 2 demonstrates the high accuracy of the trained estimator. We defer the architecture and optimization details to Appendix E.

While in this paper we focus on the degradation estimator’s benefits for likelihood approximation, one may leverage this estimator for additional applications. As an example, we estimate the degradations’ parameters in the real-world datasets LFW-Test [22], WebPhoto-Test [61], and WIDER-Test [68, 75] and approximate their distribution using Kernel Density Estimation (KDE). Then, we synthesize degraded measurements from CelebA-Test [25, 33, 75], a dataset of clean images, by sampling A according to the predicted distribution corresponding to each real-world dataset. The resulting synthetic datasets mimic the real-world ones, and therefore enable a more appropriate evaluation of real-world image restoration algorithms. This stands in contrast with prior works that sample the parameters of A uniformly [16, 31, 61, 66, 69, 75]. Hence, we utilize our synthetic datasets (as well as uniform sampling) to evaluate the

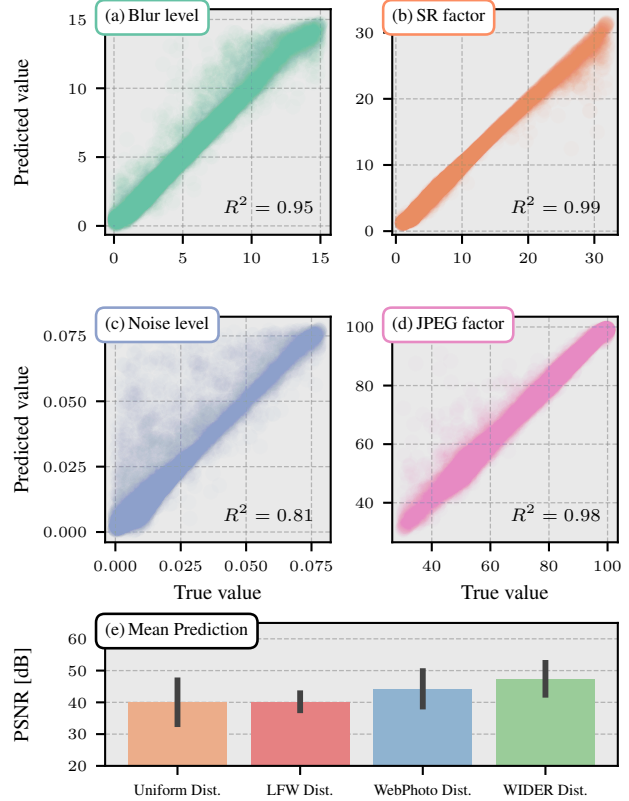


Figure 2. **Degradation estimator accuracy.** We test our degradation estimator on synthetic CelebA-Test datasets (Section 3.2). (a-d) Scatter plots and R^2 scores of the true vs. the predicted values for each type of operator in Eq. (1). (e) The mean and standard deviation of the PSNR between $\mu_Y(x, a)$ and $\mu_Y(x, a_\theta(y))$. The estimator demonstrates high prediction accuracy, as reflected by the high PSNR and R^2 scores.

proposed tools presented in the next sections. In Figure 3 we plot the approximated distributions of the real-world degradations’ parameters, and in Appendix F.2 we compare the results visually.

3.3. Blind measure of consistency

An immediate application of Eq. (3) is a *blind* consistency measure. In the case where the true degradation process a is known, we define

$$\text{CMSE}(\hat{X}) := \mathbb{E}_{(\hat{x}, y) \sim p_{\hat{X}, Y}} [\|y - \mu_Y(\hat{x}, a)\|_2^2]. \quad (5)$$

This is a direct generalization of the commonly used consistency measure, as practiced in [1, 27, 36–39, 44, 45]. In real-world scenarios where a is unknown, we use the approximation of $\ell(y, x)$ in Eq. (4) and define

$$\text{ProxCMSE}(\hat{X}) := \mathbb{E}_{(\hat{x}, y) \sim p_{\hat{X}, Y}} [\|y - \mu_Y(\hat{x}, a_\theta(y))\|_2^2]. \quad (6)$$

Namely, if $a_\theta(y)$ is trained appropriately, $\text{ProxCMSE}(\hat{X})$ would be an approximation of $\text{CMSE}(\hat{X})$. In Figure 4 we

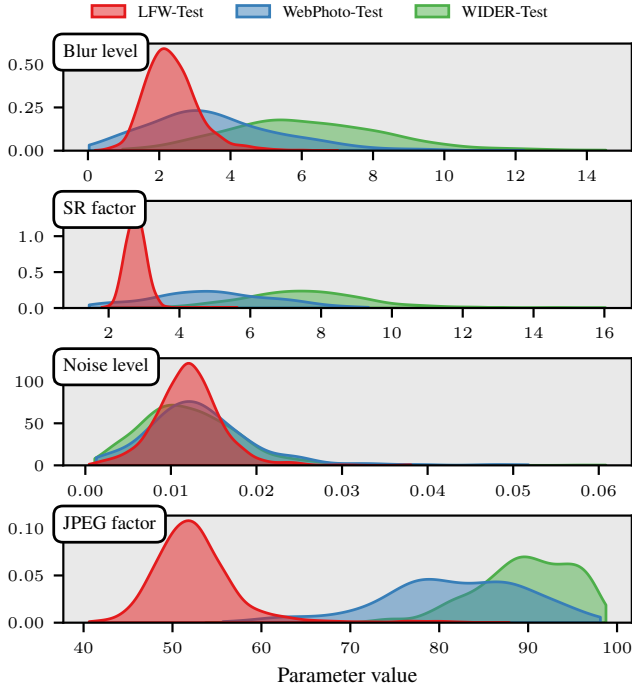


Figure 3. **Degrations in real-world BFR datasets.** Using our degradation estimator, we reveal the distribution of the degradations presented in real-world datasets. This information can be utilized to better analyze such datasets, as well as mimicking them.

show that ProxCMSE aligns well with the true CMSE on the datasets we synthesized in Section 3.2. In Tables 1 and 2 we use ProxCMSE as another measure to evaluate algorithms on real-world datasets.

3.4. Plug-and-play real-world image restoration

Another application of our degradation estimator and the derived likelihood approximation is the ability to construct plug-and-play blind restoration algorithms that harness pre-trained generative image priors, such as diffusion models. To achieve valid and perceptually pleasing restorations in blind face restoration, prior plug-and-play diffusion methods use different types of heuristics. PGDiff [67] uses the guidance term $\nabla_{\hat{x}} \|\hat{x} - f(y)\|$ at each step, where $f(y)$ is an MMSE predictor of X from $Y = y$. DifFace [69] starts from an intermediate diffusion timestep, initialized by $f(y)$ with no guidance term. As seen in Figure 5, these heuristics tend to produce inconsistent outputs.

Here, we present a new approach: *Empirical Likelihood Approximation with Diffusion prior* (ELAD) (Algorithm 1). Our algorithm extends DifFace by guiding the diffusion process to take steps in the direction of the approximated log-likelihood score. Thus, our approach is similar to DPS [8], where we use our approximation of the likelihood (Eq. (4)) instead of the true one, $\log p_{Y|X}(y|x)$ (which

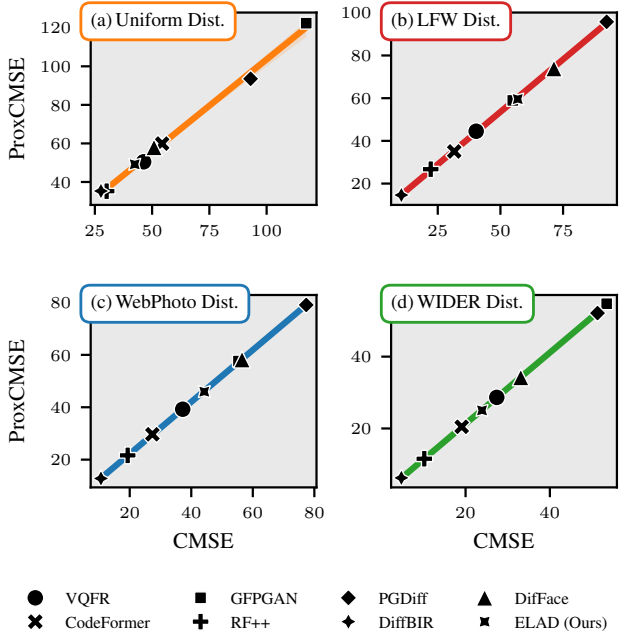


Figure 4. **Proxy consistency measure.** Each plot shows the CMSE versus ProxCMSE, evaluated on synthetic CelebA-Test datasets (Section 3.2). The strong alignment of the two suggests that ProxCMSE is a trustworthy approximation for the CMSE when the degradation process is unknown.

is unavailable in our setting). As seen in Figure 5, using such guidance promotes consistency with the measurement at each step without sacrificing image quality. We perform 100 denoising steps like DifFace, starting from an intermediate timestep for accelerated sampling. While we adapt DifFace’s diffusion prior, note that our method is not limited only for such a prior. Namely, the results could be further improved by using better priors. See Appendix E for more implementation details.

We defer the quantitative evaluation of ELAD on synthetic and real-world datasets to Section 4.3, immediately after we introduce our new proxy distortion measures. A qualitative comparison between ELAD and leading end-to-end methods on real-world datasets is presented in Figure 6.

4. Proxy distortion measures

This section introduces the *Proxy Mean Squared Error* (ProxMSE), a distortion measure that allows to practically rank image restoration algorithms according to their MSE without access to the ground-truth images. Using the same derivations, we present ProxLPIPS as a no-reference perceptual distortion measure. We start by defining distortion measures in general and MSE and LPIPS in particular. We continue by defining ProxMSE and ProxLPIPS, showing why they produce rankings that are faithful to the true MSE

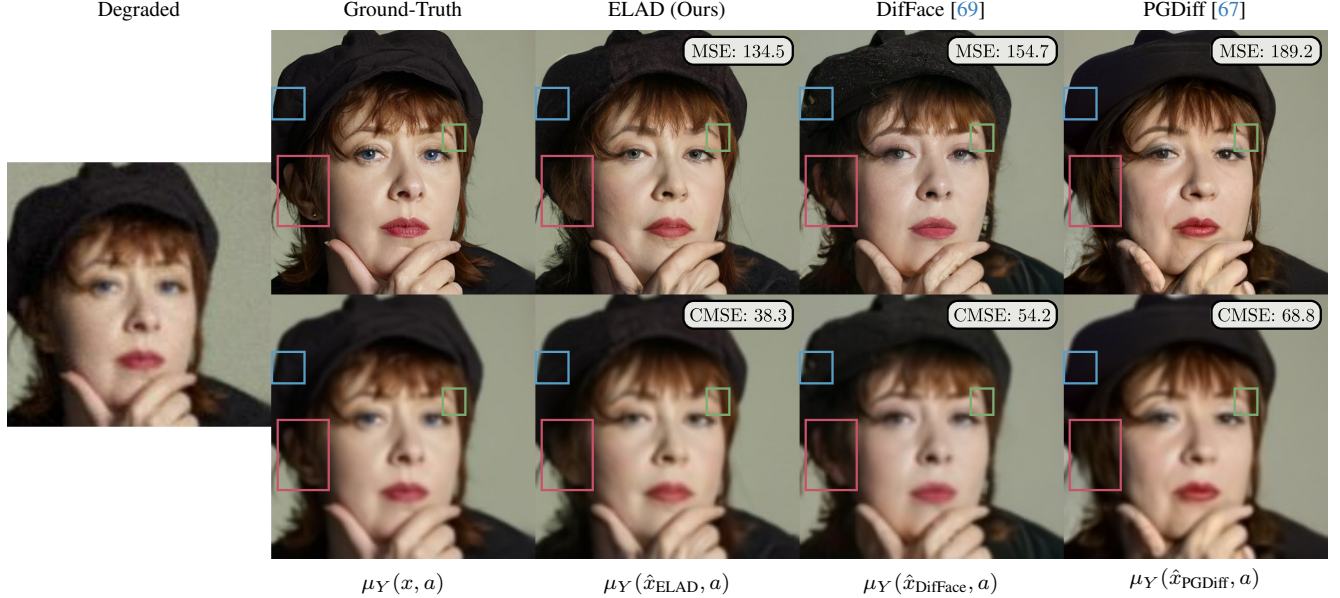


Figure 5. **Consistency of P&P real-world restoration methods.** Left column: A synthetic degraded example from CelebA-Test. First row: The ground-truth image alongside the restorations of ELAD (our method), DiffFace, and PGDiff. Second row: The mean of the likelihood defined using the true degradation process a and the corresponding image from the row above. For reference, we also report the MSE and CMSE of each method (Eq. (5)). As shown, ELAD attains better consistency with the measurement. PGDiff, for example, does not restore the ear (red rectangle), which is visible both in the degraded image and in $\mu_Y(x, a)$. Similarly, DiffFace erases part of the brow (green rectangle) and creates inconsistent artifacts in the hat (blue rectangle). In contrast, ELAD performs better by guiding the diffusion process to produce consistent reconstructions. As a positive side effect, achieving better consistency also leads to better distortion, which is apparent visually in the top row, and can be confirmed by the reported MSE and by Table 1.

Algorithm 1: ELAD - Blind Restoration Diffusion Sampler (a full version is given in Appendix E)

Input: measurement y , degradation estimator a_θ ,
MMSE regressor f , start time $T_0 \leq T$,
step sizes $\{\lambda_t\}_{t=1}^{T_0}$

Output: a restored image x_0

- 1 $x_{T_0} = \text{AddNoise}(f(y), T_0)$
 - 2 $\hat{a} = a_\theta(y)$ // predict degradation
 - 3 **for** $t = T_0$ **to** 1 **do**
 - 4 $\hat{x}_0^t = \text{DenoiseStep}(x_t)$
 // compute score likelihood
 - 5 $g = \nabla_{\hat{x}_t} \|y - \mu(\hat{x}_0^t, \hat{a})\|_2^2$
 // perform likelihood step
 - 6 $\hat{x}_0^t = \hat{x}_0^t - \lambda_t \cdot g.\text{clamp}(-1, 1)$
 - 7 $x_{t-1} = \text{DDIMStep}(x_t, \hat{x}_0^t)$
 - 8 **end**
-

and LPIPS. Then, we demonstrate that ProxMSE and ProxLPIPS are highly correlative to the true MSE and LPIPS by conducting controlled experiments on synthetic degradations. Finally, we utilize ProxMSE and ProxLPIPS to rank several real-world face restoration algorithms.

4.1. Background

Non-blind image restoration algorithms are typically evaluated by full-reference distortion measures, which quantify the discrepancy between the reconstructed images and the ground-truth ones. Formally, the average distortion of an estimator \hat{X} is defined by

$$\mathbb{E}_{(x, \hat{x}) \sim p_{X, \hat{X}}} [\Delta(x, \hat{x})], \quad (7)$$

where $\Delta(x, \hat{x})$ is some distortion measure (e.g., the squared error). Thus, measuring the average distortion in practice requires access to pairs of samples from $p_{X, \hat{X}}$. The most common way to obtain such pairs is to degrade the given samples from p_X according to $p_{Y|X}$ (e.g., add noise), and then reconstruct the results using \hat{X} . Yet, in real-world scenarios, there is no access to $p_{Y|X}$, so evaluating the distortion in such cases is impossible.

Two prominent examples of distortion measures are (1) the squared error $\Delta_{\text{SE}}(x, \hat{x}) = \|x - \hat{x}\|_2^2$; and (2) LPIPS [73], a full-reference (perceptual) distortion measure that compares weighted features extracted from neural networks such as VGG [53]. In Appendix D we show that LPIPS can be interpreted as a squared error in latent space. Denoting by z the feature vector corresponding to x , we have $\Delta_{\text{LPIPS}}(x, \hat{x}) = \Delta_{\text{SE}}(z, \hat{z})$.

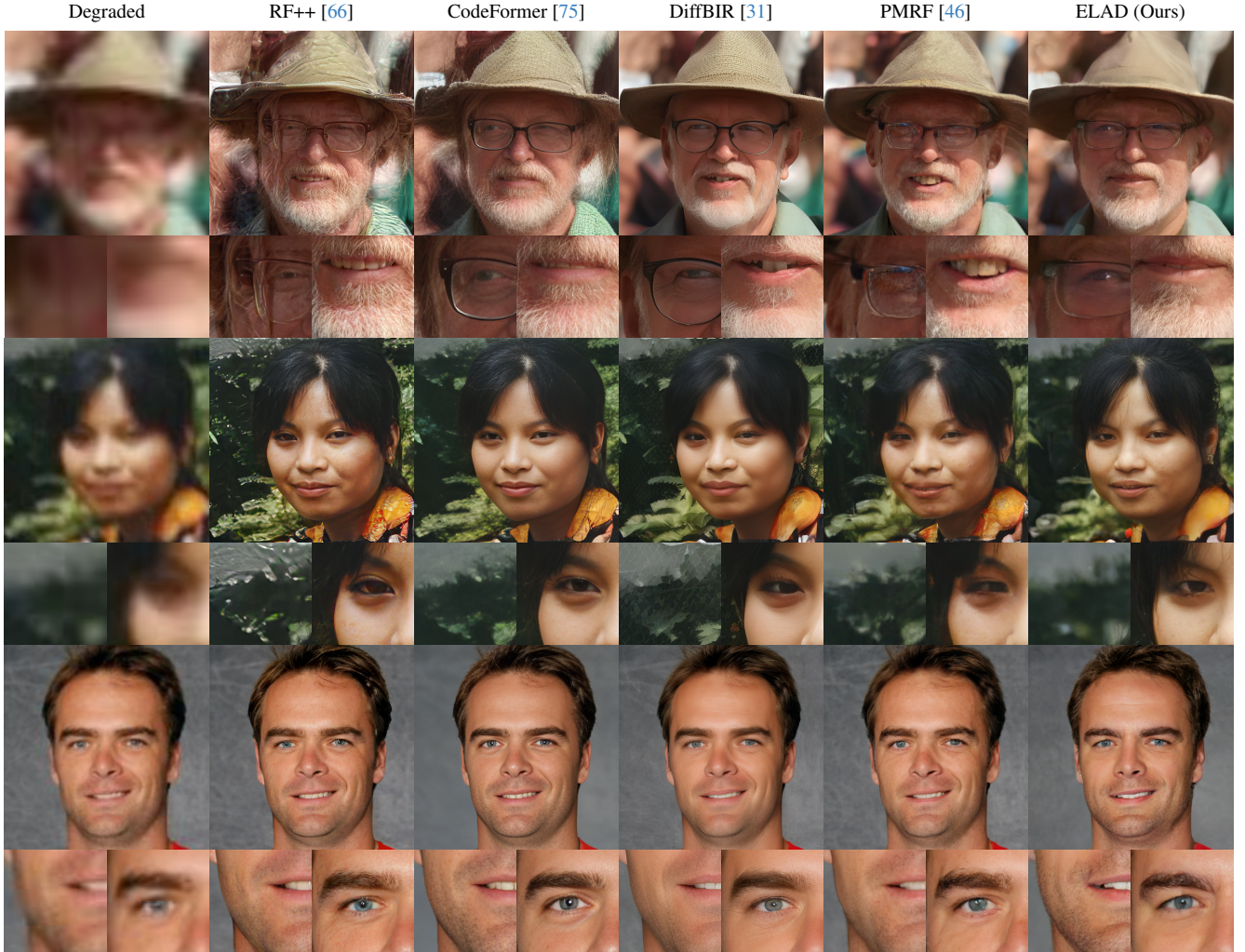


Figure 6. Restoration examples of real-world images taken from WIDER-Test, WebPhoto-Test, and LFW-Test (top to bottom) for different methods. ELAD is highly competitive against current state-of-the-art end-to-end methods while being independent of the underlying prior.

4.2. Derivation

Let \hat{X} be some estimator, and let $X^* = \mathbb{E}[X|Y]$ be the posterior mean (the MMSE estimator). We define

$$\text{ProxMSE}(\hat{X}) := \mathbb{E}_{(\hat{x}, x^*) \sim p_{\hat{X}, X^*}} [\|\hat{x} - x^*\|_2^2], \quad (8)$$

where the right hand side is the MSE between \hat{X} and X^* . Interestingly, ProxMSE satisfies the following appealing property (the proof is deferred to Appendix B):

Proposition 1. *The ProxMSE and the MSE of an estimator \hat{X} are equal up to a constant which does not depend on \hat{X} ,*

$$\text{ProxMSE}(\hat{X}) = \text{MSE}(X, \hat{X}) - d^*. \quad (9)$$

Namely, the ranking order of estimators according to their ProxMSE is equivalent to that according to their MSE.

Note that Eq. (9) was originally proved by Freirich et al. [14] (Lemma 2, Appendix B.1). Ohayon et al. [46] used $\text{ProxMSE}(\hat{X})$ as a no-reference distortion measure, but did not assess its practical validity in experiments.

In practice, we do not have access to the true MMSE estimator, but rather to an approximation of it (typically a neural network trained to minimize the MSE). In Appendix C we develop a bound on this approximation. Lastly, since LPIPS is just a MSE in latent space, we similarly define

$$\text{ProxLPIPS}(\hat{X}) := \mathbb{E}_{(\hat{z}, z^*) \sim p_{\hat{Z}, Z^*}} [\|\hat{z} - z^*\|_2^2], \quad (10)$$

where Z^* is the MMSE estimator *in the latent space*, which again is approximated using a neural network trained to minimize the LPIPS loss.

Method	LFW-Test				WebPhoto-Test				WIDER-Test			
	FID ↓	Proxy MSE ↓	Proxy LPIPS ↓	Proxy CMSE ↓	FID ↓	Proxy MSE ↓	Proxy LPIPS ↓	Proxy CMSE ↓	FID ↓	Proxy MSE ↓	Proxy LPIPS ↓	Proxy CMSE ↓
PGDiff [67]	43.52	195.20	0.319	99.0	84.94	225.7	0.368	90.4	42.60	326.9	0.373	80.9
DifFace [69]	47.39	131.0	0.319	76.7	80.88	108.3	0.354	60.6	37.03	113.6	0.334	49.7
ELAD (Ours)	46.02	114.0	0.306	62.4	81.89	92.7	0.343	48.3	37.50	101.3	0.328	39.8

Table 1. Quantitative comparison between plug-and-play diffusion methods: PGDiff, DifFace, and ELAD on real-world BFR datasets. We highlight the **first** and **second** best-performing methods in each measure. ELAD is better in terms of distortion (ProxMSE, ProxLPIPS) and consistency (ProxCMSE), with minimal impact on perception (FID).

4.3. Experiments

We use the BFR regressor of DifFace [69] as our approximate MMSE estimator. This model was trained on the synthetic degradation process defined in Eq. (1). For ProxLPIPS, we re-train the same model with an LPIPS loss: the VGG network is used to extract image features and the rest of the training scheme follows that of DifFace’s regressor.

Synthetic datasets. In Figure 7 we compare the proxy measures with their true counterparts (*e.g.*, ProxMSE vs. MSE) on the synthetic datasets presented in Section 3.2. The figure shows that ProxMSE aligns well with MSE, implying that it is a reliable, no-reference proxy MSE measure. Similarly, ProxLPIPS displays an excellent alignment with LPIPS, but it is not as accurate as ProxMSE. We hypothesize that a better alignment might be possible with a better-trained LPIPS estimator.

Real-world datasets. After establishing that ProxMSE and ProxLPIPS can serve as reliable proxy measures of MSE and LPIPS, respectively, we turn to evaluate existing real-world image restoration methods on datasets where MSE and LPIPS are impossible to compute. Table 2 in Appendix A compares state-of-the-art **end-to-end** methods on the LFW-Test, WebPhoto-Test, and WIDER-Test datasets. PMRF [46] stands out in ProxMSE and ProxCMSE, which comes with no surprise as the method is trained to achieve the best MSE possible under a perfect perceptual index constraint. Regarding perception alone, DiffBIR [31] and RestorFormer++ [66] generally lead. Note that such a comparison is impossible with prior no-reference quality measures, as those typically do not correlate with the distortion.

ELAD evaluation. Both in synthetic (Figures 4 and 7) and real-world datasets (Table 1), ELAD improves the consistency over DifFace [69] and PGDiff [67] considerably, as reflected by the (Prox)CMSE. A somewhat surprising side-effect of the improved consistency is an improved distortion performance, as seen by (Prox)MSE and (Prox)LPIPS. The slight decrease in FID compared to DifFace is expected as we add a guidance term that may compete with the unconditional generative prior. As seen in Figures 5 and 6, this

decrease is not noticeable. In fact, ELAD is highly competitive in terms of perceptual quality compared to end-to-end methods (see Figure 6). All in all, ELAD is the state-of-the-art plug-and-play method for BFR tasks.

5. Related work

Degradation estimation and its application. The idea of identifying the degradations that a given image has gone through was previously explored in the literature in different contexts. In [5], a classifier was trained to determine which degradation is present in a given image, out of 4 possibilities (rain, haze, noise, low-light). An image captioner was trained in [24] to produce the list of degradations from an image, and a coarse description of their severity (*e.g.*, high amount of noise, low amount of blur). These methods neglect the *order* and the exact parameters’ *values* of each degradation. Another line of work [42, 49, 57] learns the latent representation of degradations in an unsupervised manner. In all of the above, the identified degradation is used as an additional input condition for the restoration algorithm. This is fundamentally different than our approach, as we do not train an algorithm conditioned on the predicted degradations, but rather use the estimated degradations to approximate the likelihood. In [4], camera sensor noise was modeled and fitted as a heteroscedastic Gaussian distribution to mimic a real-world noisy dataset, and [23, 52] optimized a down-sampling kernel per-image. Both are not applicable to a more complex chain of degradations.

Consistency. Measuring the consistency of the reconstructions with the inputs is common for non-blind image restoration tasks, such as noiseless super-resolution and JPEG decoding [1, 2, 36–39]. The work in [27, 44] considered the consistency in noisy problems to be testing the residual image between the degraded input and the restored output for normality. Ohayon et al. [45] generalized this notion as a requirement for the similarity between the conditional distributions $p_{Y|X}$ and $p_{Y|\hat{X}}$. However, $p_{Y|X}$ is unknown in blind restoration tasks.

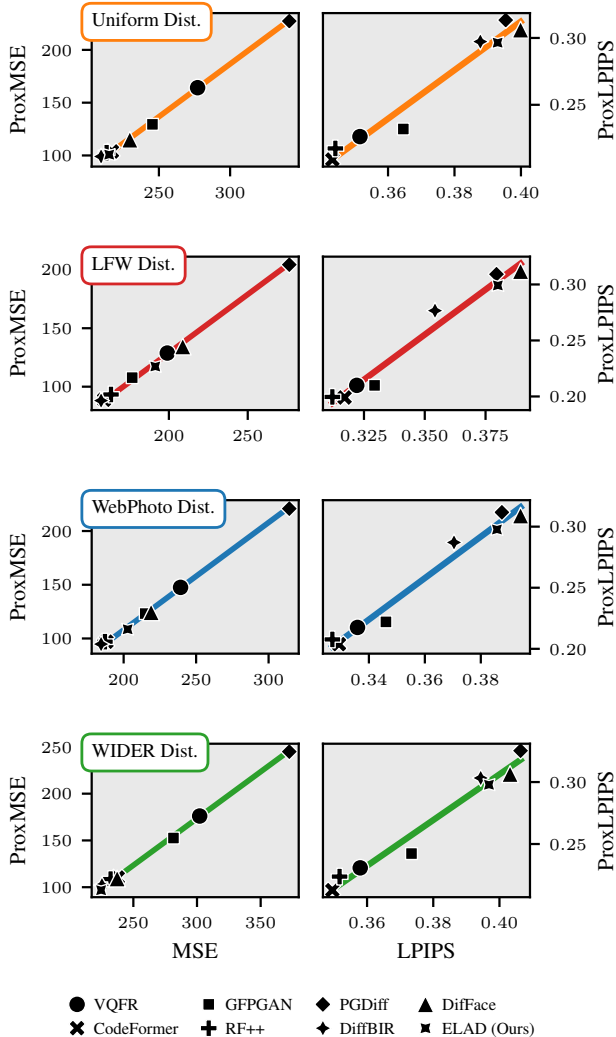


Figure 7. **Proxy distortion measures.** The plots compare the proxy measures with their true counterparts, for several state-of-the-art methods evaluated on the synthetic CelebA-Test datasets (Section 3.2). A linear regression line is drawn for better clarity (for ProxMSE the slope equals one, following Proposition 1). ProxMSE and ProxLPIPS rank methods similarly to the MSE and LPIPS measures without the need for ground-truth images.

Plug & play image restoration. Blind plug-and-play methods typically assume a simple parametric family of degradations (*e.g.*, convolution with a fixed-sized kernel), and attempt to jointly estimate the degradation’s parameters (*e.g.*, the kernel’s weights) and the clean image [9, 29, 43, 58]. Such parametric families are typically too narrow to describe complex degradations that may occur in practice (*e.g.*, compression artifacts). Another line of work utilizes heuristic guidance terms and initialization schemes to generate images using a generative model, such that the generated outputs share the same features with the given de-

graded measurement [67, 69]. Due to the heuristic nature of such methods, the restored images may “over-fit” the degraded inputs and produce artifacts, or “under-fit” them and become inconsistent.

Blind (no-reference) performance measures. Evaluating real-world image restoration methods is commonly done using no-reference quality measures (*e.g.* NIQE [41], NIMA [56], ClipIQA [60]) or statistical divergences (*e.g.*, FID [51], KID [20]). All of these measures do not consider the given degraded inputs. In other words, they may even highly reward a restoration algorithm for producing outputs that are entirely inconsistent with the inputs.

Real-world paired datasets. Another way to evaluate real-world image restoration algorithms is to construct datasets that consist of pairs of low and high-quality images, *e.g.*, where the first is acquired with a mobile phone and the second with a high-quality DSLR camera [19, 23, 47, 74]. This approach is too costly, and may not faithfully represent the distribution of real-world degraded images [61, 62, 75].

6. Conclusion and limitations

This work aimed to provide practical tools to help foster progress in a highly challenging task: Real-world image restoration. We proposed ELA, a new approach to approximate the consistency of a reconstructed candidate with a given degraded image. Our method relies on a novel degradation estimator, which we train to predict the chain of degradations that a given degraded image has gone through. Using ELA, we directly define measures of consistency for real-world image restoration algorithms (Prox)CMSE, and develop ELAD: a new plug-and-play real-world image restoration algorithm that beats its predecessors. Moreover, our proposed ProxMSE and ProxLPIPS measures offer a new way to indicate the *distortion* of real-world image restoration methods, without any access to the ground-truth images. While our work provides new effective tools for real-world image restoration, it also has several limitations. First, the parametrization of the degradation family may limit the effectiveness of the degradation estimator. For example, some images in WebPhoto seem to contain haze (see, *e.g.*, Appendix F.2), which is not accounted in Eq. (1). Second, ELA utilizes a degradation predictor to approximate the mean of $p_{Y|X}$, yet it is possible that many different degradations correspond to a given degraded image. A more faithful approximation could be one that averages over such space of possible degradations. Third, our proxy measures assumes access to accurate approximations of MMSE estimators. While in Appendix C we provide an upper bound for the error of such a measure, the tightness of this bound remains unclear in practice. Apart from addressing the above limitations, follow-up work could explore a multitude of different directions, such as (*i*) testing our tools on other real-world tasks such as blind super-resolution (BSR),

and (ii) training and evaluating other methods (*e.g.*, CodeFormer or DiffBIR) on synthetic datasets that mimic real-world ones (as described in Sec. 3.2).

Acknowledgment. We thank Hila Manor and Noam Elata for proofreading an earlier version of the paper.

References

- [1] Yuval Bahat and Tomer Michaeli. Explorable Super Resolution. In *Proceedings of the IEEE/CVF Conference on Computer Vision and Pattern Recognition*, pages 2716–2725, 2020. [3](#), [7](#)
- [2] Yuval Bahat and Tomer Michaeli. What’s in the Image? Explorable Decoding of Compressed Images. In *Proceedings of the IEEE/CVF Conference on Computer Vision and Pattern Recognition*, pages 2908–2917, 2021. [7](#)
- [3] Yochai Blau and Tomer Michaeli. The Perception-Distortion Tradeoff. In *Proceedings of the IEEE Conference on Computer Vision and Pattern Recognition*, pages 6228–6237, 2018. [2](#)
- [4] Tim Brooks, Ben Mildenhall, Tianfan Xue, Jiawen Chen, Dillon Sharlet, and Jonathan T. Barron. Unprocessing Images for Learned Raw Denoising. In *Proceedings of the IEEE/CVF Conference on Computer Vision and Pattern Recognition*, pages 11036–11045, 2019. [7](#)
- [5] Jin Cao, Deyu Meng, and Xiangyong Cao. Chain-of-Restoration: Multi-Task Image Restoration Models are Zero-Shot Step-by-Step Universal Image Restorers. (arXiv:2410.08688), 2024. [7](#)
- [6] Xiaoxu Chen, Jingfan Tan, Tao Wang, Kaihao Zhang, Wenhan Luo, and Xiaochun Cao. Towards Real-World Blind Face Restoration with Generative Diffusion Prior. (arXiv:2312.15736), 2024. [7](#), [8](#), [9](#), [10](#)
- [7] Yunjin Chen and Thomas Pock. Trainable Nonlinear Reaction Diffusion: A Flexible Framework for Fast and Effective Image Restoration. *IEEE Transactions on Pattern Analysis and Machine Intelligence*, 39(6):1256–1272, 2017. [1](#)
- [8] Hyungjin Chung, Jeongsol Kim, Michael Thompson McCann, Marc Louis Klasky, and Jong Chul Ye. Diffusion Posterior Sampling for General Noisy Inverse Problems. In *The Eleventh International Conference on Learning Representations*, 2022. [2](#), [4](#), [5](#)
- [9] Hyungjin Chung, Jeongsol Kim, Sehui Kim, and Jong Chul Ye. Parallel Diffusion Models of Operator and Image for Blind Inverse Problems. In *Proceedings of the IEEE/CVF Conference on Computer Vision and Pattern Recognition*, pages 6059–6069, 2023. [8](#)
- [10] Kostadin Dabov, Alessandro Foi, Vladimir Katkovnik, and Karen Egiazarian. Image Denoising by Sparse 3-D Transform-Domain Collaborative Filtering. *IEEE Transactions on Image Processing*, 16(8):2080–2095, 2007. [1](#)
- [11] Jia Deng, Wei Dong, Richard Socher, Li-Jia Li, Kai Li, and Li Fei-Fei. ImageNet: A large-scale hierarchical image database. In *2009 IEEE Conference on Computer Vision and Pattern Recognition*, pages 248–255, 2009. [3](#)
- [12] Michael Elad and Michal Aharon. Image Denoising Via Sparse and Redundant Representations Over Learned Dictionaries. *IEEE Transactions on Image Processing*, 15(12):3736–3745, 2006. [1](#)
- [13] Michael Elad, Bahjat Kawar, and Gregory Vaksman. Image Denoising: The Deep Learning Revolution and Beyond—A Survey Paper. *SIAM Journal on Imaging Sciences*, 16(3):1594–1654, 2023. [1](#)
- [14] Dror Freirich, Tomer Michaeli, and Ron Meir. A Theory of the Distortion-Perception Tradeoff in Wasserstein Space. In *Advances in Neural Information Processing Systems*, pages 25661–25672. Curran Associates, Inc., 2021. [6](#), [1](#)
- [15] Shuhang Gu, Lei Zhang, Wangmeng Zuo, and Xiangchu Feng. Weighted Nuclear Norm Minimization with Application to Image Denoising. In *Proceedings of the IEEE Conference on Computer Vision and Pattern Recognition*, pages 2862–2869, 2014. [1](#)
- [16] Yuchao Gu, Xintao Wang, Liangbin Xie, Chao Dong, Gen Li, Ying Shan, and Ming-Ming Cheng. VQFR: Blind Face Restoration with Vector-Quantized Dictionary and Parallel Decoder. In *Computer Vision – ECCV 2022*, pages 126–143, Cham, 2022. Springer Nature Switzerland. [2](#), [3](#), [1](#), [4](#), [7](#), [8](#), [9](#), [10](#)
- [17] Javier Gurrola-Ramos, Oscar Dalmau, and Teresa E. Alarcón. A Residual Dense U-Net Neural Network for Image Denoising. *IEEE Access*, 9:31742–31754, 2021. [1](#)
- [18] Alexander Hägele, Elie Bakouch, Atli Kosson, Loubna Ben Allal, Leandro Von Werra, and Martin Jaggi. Scaling Laws and Compute-Optimal Training Beyond Fixed Training Durations. (arXiv:2405.18392), 2024. [3](#)
- [19] Junlin Han, Mehrdad Shoeiby, Tim Malthus, Elizabeth Botha, Janet Anstee, Saeed Anwar, Ran Wei, Mohammad Ali Armin, Hongdong Li, and Lars Petersson. Underwater image restoration via contrastive learning and a real-world dataset. *Remote Sensing*, 14(4297), 2022. [8](#)
- [20] Martin Heusel, Hubert Ramsauer, Thomas Unterthiner, Bernhard Nessler, and Sepp Hochreiter. GANs Trained by a Two Time-Scale Update Rule Converge to a Local Nash Equilibrium. In *Advances in Neural Information Processing Systems*. Curran Associates, Inc., 2017. [8](#), [1](#)
- [21] Jonathan Ho, Ajay Jain, and Pieter Abbeel. Denoising Diffusion Probabilistic Models. In *Advances in Neural Information Processing Systems*, pages 6840–6851. Curran Associates, Inc., 2020. [5](#)
- [22] Gary B. Huang, Manu Ramesh, Tamara Berg, and Erik Learned-Miller. Labeled faces in the wild: A database for studying face recognition in unconstrained environments. Technical Report 07-49, University of Massachusetts, Amherst, 2007. [3](#), [8](#)
- [23] Xiaozhong Ji, Yun Cao, Ying Tai, Chengjie Wang, Jilin Li, and Feiyue Huang. Real-world super-resolution via kernel estimation and noise injection. In *The IEEE/CVF Conference on Computer Vision and Pattern Recognition (CVPR) Workshops*, 2020. [2](#), [7](#), [8](#)
- [24] Aiwen Jiang, Zhi Wei, Long Peng, Feiqiang Liu, Wenbo Li, and Mingwen Wang. DaLPSR: Leverage Degradation-Aligned Language Prompt for Real-World Image Super-Resolution. (arXiv:2406.16477), 2024. [7](#)
- [25] Tero Karras, Timo Aila, Samuli Laine, and Jaakko Lehtinen. Progressive Growing of GANs for Improved Quality, Stability, and Variation. In *International Conference on Learning Representations*, 2018. [3](#)
- [26] Tero Karras, Samuli Laine, and Timo Aila. A Style-Based Generator Architecture for Generative Adversarial Networks. In *Proceedings of the IEEE/CVF Conference*

- on *Computer Vision and Pattern Recognition*, pages 4401–4410, 2019. 3
- [27] Bahjat Kawar, Gregory Vaksman, and Michael Elad. Stochastic Image Denoising by Sampling From the Posterior Distribution. In *Proceedings of the IEEE/CVF International Conference on Computer Vision*, pages 1866–1875, 2021. 1, 2, 3, 7
- [28] Bahjat Kawar, Michael Elad, Stefano Ermon, and Jiaming Song. Denoising Diffusion Restoration Models. *Advances in Neural Information Processing Systems*, 35:23593–23606, 2022. 2
- [29] Charles Laroche, Andrés Almansa, and Eva Coupeté. Fast Diffusion EM: A Diffusion Model for Blind Inverse Problems With Application to Deconvolution. In *Proceedings of the IEEE/CVF Winter Conference on Applications of Computer Vision*, pages 5271–5281, 2024. 8
- [30] Jingyun Liang, Jiezhong Cao, Guolei Sun, Kai Zhang, Luc Van Gool, and Radu Timofte. SwinIR: Image Restoration Using Swin Transformer. In *Proceedings of the IEEE/CVF International Conference on Computer Vision*, pages 1833–1844, 2021. 1
- [31] Xinqi Lin, Jingwen He, Ziyang Chen, Zhaoyang Lyu, Bo Dai, Fanghua Yu, Wanli Ouyang, Yu Qiao, and Chao Dong. DiffBIR: Towards Blind Image Restoration with Generative Diffusion Prior. (arXiv:2308.15070), 2024. 2, 3, 6, 7, 1, 4, 8, 9, 10
- [32] Chang Liu, Yinpeng Dong, Wenzhao Xiang, Xiao Yang, Hang Su, Jun Zhu, Yuefeng Chen, Yuan He, Hui Xue, and Shihao Zheng. A Comprehensive Study on Robustness of Image Classification Models: Benchmarking and Rethinking. *International Journal of Computer Vision*, 2024. 3
- [33] Ziwei Liu, Ping Luo, Xiaogang Wang, and Xiaoou Tang. Deep learning face attributes in the wild. In *Proceedings of International Conference on Computer Vision (ICCV)*, 2015. 3
- [34] Zhuang Liu, Hanzi Mao, Chao-Yuan Wu, Christoph Feichtenhofer, Trevor Darrell, and Saining Xie. A ConvNet for the 2020s. In *Proceedings of the IEEE/CVF Conference on Computer Vision and Pattern Recognition*, pages 11976–11986, 2022. 3
- [35] Ilya Loshchilov and Frank Hutter. Decoupled Weight Decay Regularization. In *International Conference on Learning Representations*, 2018. 3
- [36] Andreas Lugmayr, Martin Danelljan, Luc Van Gool, and Radu Timofte. SRFlow: Learning the Super-Resolution Space with Normalizing Flow. In *Computer Vision – ECCV 2020*, pages 715–732, Cham, 2020. Springer International Publishing. 3, 7
- [37] Andreas Lugmayr, Martin Danelljan, and Radu Timofte. NTIRE 2021 Learning the Super-Resolution Space Challenge. In *Proceedings of the IEEE/CVF Conference on Computer Vision and Pattern Recognition*, pages 596–612, 2021.
- [38] Andreas Lugmayr, Martin Danelljan, Radu Timofte, Kangwook Kim, Younggeun Kim, Jae-young Lee, Zechao Li, Jinshan Pan, Dongseok Shim, Ki-Ung Song, Jinhui Tang, Cong Wang, and Zhihao Zhao. NTIRE 2022 Challenge on Learning the Super-Resolution Space. In *Proceedings of the IEEE/CVF Conference on Computer Vision and Pattern Recognition*, pages 786–797, 2022.
- [39] Sean Man, Guy Ohayon, Theo Adrai, and Michael Elad. High-Perceptual Quality JPEG Decoding via Posterior Sampling. In *Proceedings of the IEEE/CVF Conference on Computer Vision and Pattern Recognition*, pages 1272–1282, 2023. 3, 7
- [40] Morteza Mardani, Jiaming Song, Jan Kautz, and Arash Vahdat. A Variational Perspective on Solving Inverse Problems with Diffusion Models. In *The Twelfth International Conference on Learning Representations*, 2023. 2
- [41] Anish Mittal, Rajiv Soundararajan, and Alan C. Bovik. Making a “completely blind” image quality analyzer. *IEEE Signal Processing Letters*, 20(3):209–212, 2013. 8
- [42] Chong Mou, Yanze Wu, Xintao Wang, Chao Dong, Jian Zhang, and Ying Shan. Metric Learning Based Interactive Modulation for Real-World Super-Resolution. In *Computer Vision – ECCV 2022*, pages 723–740, Cham, 2022. Springer Nature Switzerland. 2, 7
- [43] Naoki Murata, Koichi Saito, Chieh-Hsin Lai, Yuhta Takida, Toshimitsu Uesaka, Yuki Mitsufuji, and Stefano Ermon. GibbsDDRM: A Partially Collapsed Gibbs Sampler for Solving Blind Inverse Problems with Denoising Diffusion Restoration. In *Proceedings of the 40th International Conference on Machine Learning*, pages 25501–25522. PMLR, 2023. 8
- [44] Guy Ohayon, Theo Adrai, Gregory Vaksman, Michael Elad, and Peyman Milanfar. High Perceptual Quality Image Denoising With a Posterior Sampling CGAN. In *Proceedings of the IEEE/CVF International Conference on Computer Vision*, pages 1805–1813, 2021. 1, 3, 7
- [45] Guy Ohayon, Theo Joseph Adrai, Michael Elad, and Tomer Michaeli. Reasons for the Superiority of Stochastic Estimators over Deterministic Ones: Robustness, Consistency and Perceptual Quality. In *Proceedings of the 40th International Conference on Machine Learning*, pages 26474–26494. PMLR, 2023. 3, 7
- [46] Guy Ohayon, Tomer Michaeli, and Michael Elad. Posterior-Mean Rectified Flow: Towards Minimum MSE Photo-Realistic Image Restoration. (arXiv:2410.00418), 2024. 6, 7, 1, 8, 9, 10
- [47] Tobias Plotz and Stefan Roth. Benchmarking Denoising Algorithms With Real Photographs. In *Proceedings of the IEEE Conference on Computer Vision and Pattern Recognition*, pages 1586–1595, 2017. 8
- [48] Yaniv Romano, Michael Elad, and Peyman Milanfar. The Little Engine That Could: Regularization by Denoising (RED). *SIAM Journal on Imaging Sciences*, 10(4):1804–1844, 2017. 2
- [49] Andrés Romero, Luc Van Gool, and Radu Timofte. Unpaired Real-World Super-Resolution With Pseudo Controllable Restoration. In *Proceedings of the IEEE/CVF Conference on Computer Vision and Pattern Recognition*, pages 798–807, 2022. 7
- [50] Chitwan Saharia, William Chan, Saurabh Saxena, Lala Li, Jay Whang, Emily L. Denton, Kamyar Ghasemipour, Raphael Gontijo Lopes, Burcu Karagol Ayan, Tim Salimans,

- Jonathan Ho, David J. Fleet, and Mohammad Norouzi. Photorealistic Text-to-Image Diffusion Models with Deep Language Understanding. *Advances in Neural Information Processing Systems*, 35:36479–36494, 2022. 5
- [51] Mehdi S. M. Sajjadi, Olivier Bachem, Mario Lucic, Olivier Bousquet, and Sylvain Gelly. Assessing Generative Models via Precision and Recall. In *Advances in Neural Information Processing Systems*. Curran Associates, Inc., 2018. 8
- [52] Assaf Shocher, Nadav Cohen, and Michal Irani. “Zero-Shot” Super-Resolution Using Deep Internal Learning. In *Proceedings of the IEEE Conference on Computer Vision and Pattern Recognition*, pages 3118–3126, 2018. 7
- [53] Karen Simonyan and Andrew Zisserman. Very Deep Convolutional Networks for Large-Scale Image Recognition. (arXiv:1409.1556), 2015. 5
- [54] Jiaming Song, Chenlin Meng, and Stefano Ermon. Denoising Diffusion Implicit Models. In *International Conference on Learning Representations*, 2020. 3, 5
- [55] Jiaming Song, Arash Vahdat, Morteza Mardani, and Jan Kautz. Pseudoinverse-Guided Diffusion Models for Inverse Problems. In *International Conference on Learning Representations*, 2022. 5
- [56] Hossein Talebi and Peyman Milanfar. NIMA: Neural image assessment. *IEEE Transactions on Image Processing*, 27(8): 3998–4011, 2018. 8
- [57] Phong Tran, Anh Tran, Quynh Phung, and Minh Hoai. Explore Image Deblurring via Blur Kernel Space. (arXiv:2104.00317), 2021. 7
- [58] Siwei Tu, Weidong Yang, and Ben Fei. Taming Generative Diffusion for Universal Blind Image Restoration. (arXiv:2408.11287), 2024. 8
- [59] Singanallur V. Venkatakrisnan, Charles A. Bouman, and Brendt Wohlberg. Plug-and-Play priors for model based reconstruction. In *2013 IEEE Global Conference on Signal and Information Processing*, pages 945–948, 2013. 2
- [60] Jianyi Wang, Kelvin C. K. Chan, and Chen Change Loy. Exploring CLIP for Assessing the Look and Feel of Images. *Proceedings of the AAAI Conference on Artificial Intelligence*, 37(2):2555–2563, 2023. 8
- [61] Xintao Wang, Yu Li, Honglun Zhang, and Ying Shan. Towards Real-World Blind Face Restoration With Generative Facial Prior. In *Proceedings of the IEEE/CVF Conference on Computer Vision and Pattern Recognition*, pages 9168–9178, 2021. 2, 3, 8, 1, 4, 7, 9
- [62] Xintao Wang, Liangbin Xie, Chao Dong, and Ying Shan. Real-ESRGAN: Training Real-World Blind Super-Resolution With Pure Synthetic Data. In *Proceedings of the IEEE/CVF International Conference on Computer Vision*, pages 1905–1914, 2021. 2, 8
- [63] Yinhuai Wang, Jiwen Yu, and Jian Zhang. Zero-Shot Image Restoration Using Denoising Diffusion Null-Space Model. (arXiv:2212.00490), 2022. 2
- [64] Zhou Wang and Alan C. Bovik. Mean squared error: Love it or leave it? A new look at Signal Fidelity Measures. *IEEE Signal Processing Magazine*, 26(1):98–117, 2009. 1
- [65] Zhou Wang, A.C. Bovik, H.R. Sheikh, and E.P. Simoncelli. Image quality assessment: From error visibility to structural similarity. *IEEE Transactions on Image Processing*, 13(4): 600–612, 2004. 2
- [66] Zhouxia Wang, Jiawei Zhang, Tianshui Chen, Wenping Wang, and Ping Luo. RestoreFormer++: Towards Real-World Blind Face Restoration From Undegraded Key-Value Pairs. *IEEE Transactions on Pattern Analysis and Machine Intelligence*, 45(12):15462–15476, 2023. 3, 6, 7, 1, 4, 8, 9, 10
- [67] Peiqing Yang, Shangchen Zhou, Qingyi Tao, and Chen Change Loy. PGDiff: Guiding Diffusion Models for Versatile Face Restoration via Partial Guidance. *Advances in Neural Information Processing Systems*, 36: 32194–32214, 2023. 4, 5, 7, 8, 9, 10
- [68] Shuo Yang, Ping Luo, Chen-Change Loy, and Xiaoou Tang. WIDER FACE: A Face Detection Benchmark. In *Proceedings of the IEEE Conference on Computer Vision and Pattern Recognition*, pages 5525–5533, 2016. 3, 10
- [69] Zongsheng Yue and Chen Change Loy. DifFace: Blind Face Restoration with Diffused Error Contraction. (arXiv:2212.06512), 2023. 2, 3, 4, 5, 7, 8, 9, 10
- [70] Syed Waqas Zamir, Aditya Arora, Salman Khan, Munawar Hayat, Fahad Shahbaz Khan, and Ming-Hsuan Yang. Restormer: Efficient Transformer for High-Resolution Image Restoration. In *Proceedings of the IEEE/CVF Conference on Computer Vision and Pattern Recognition*, pages 5728–5739, 2022. 1
- [71] Kai Zhang, Wangmeng Zuo, Yunjin Chen, Deyu Meng, and Lei Zhang. Beyond a Gaussian Denoiser: Residual Learning of Deep CNN for Image Denoising. *IEEE Transactions on Image Processing*, 26(7):3142–3155, 2017. 1
- [72] Kai Zhang, Jingyun Liang, Luc Van Gool, and Radu Timofte. Designing a Practical Degradation Model for Deep Blind Image Super-Resolution. In *Proceedings of the IEEE/CVF International Conference on Computer Vision*, pages 4791–4800, 2021. 2
- [73] Richard Zhang, Phillip Isola, Alexei A. Efros, Eli Shechtman, and Oliver Wang. The Unreasonable Effectiveness of Deep Features as a Perceptual Metric. In *Proceedings of the IEEE Conference on Computer Vision and Pattern Recognition*, pages 586–595, 2018. 2, 5, 3
- [74] Xinyi Zhang, Hang Dong, Jinshan Pan, Chao Zhu, Ying Tai, Chengjie Wang, Jilin Li, Feiyue Huang, and Fei Wang. Learning to restore hazy video: A new real-world dataset and a new method. In *Proceedings of the IEEE/CVF Conference on Computer Vision and Pattern Recognition*, pages 9239–9248, 2021. 8
- [75] Shangchen Zhou, Kelvin Chan, Chongyi Li, and Chen Change Loy. Towards Robust Blind Face Restoration with Codebook Lookup Transformer. *Advances in Neural Information Processing Systems*, 35:30599–30611, 2022. 2, 3, 6, 8, 1, 4, 5, 7, 9, 10
- [76] Yuanzhi Zhu, Kai Zhang, Jingyun Liang, Jie Zhang Cao, Bihan Wen, Radu Timofte, and Luc Van Gool. Denoising Diffusion Models for Plug-and-Play Image Restoration. In *Proceedings of the IEEE/CVF Conference on Computer Vision and Pattern Recognition*, pages 1219–1229, 2023. 2, 5

Proxies for Distortion and Consistency with Applications for Real-World Image Restoration

Supplementary Material

A. Supplementary results

A.1. Proxy performance of real-world end-to-end methods

For completeness, we evaluate real-world blind face restoration end-to-end methods in Table 2 using the proxy measures we defined in this paper. To complement our distortion measures, we measure the perceptual quality of the reconstructions with FID [20]. It is important to note that the performance of ELAD, despite being a plug-and-play method, is not far from that of the leading end-to-end methods, as evident from Fig. 6.

A.2. CelebA-Test synthetic results

In Figures 4 and 7 in the main paper, we demonstrate the alignment between each proxy measure and its true counterpart measure on synthetic CelebA-Test datasets, using various plug-and-play and end-to-end methods. We also provide the same data in Table 3. As we noted in Sec. 4.3, a key takeaway from these results is the dominance of ELAD over the other plug-and-play methods in all measures. This is consistent with the results in Table 1.

A.3. Additional visual results

In Figures 8 to 11, we present additional restoration examples produced by various methods, including ELAD, on CelebA-Test, LFW-Test, WebPhoto-Test, and WIDER-test.

B. Proof of proposition 1

Proposition 1. *The ProxMSE and the MSE of an estimator \hat{X} are equal up to a constant which does not depend on \hat{X} ,*

$$\text{ProxMSE}(\hat{X}) = \text{MSE}(X, \hat{X}) - d^*. \quad (9)$$

Namely, the ranking order of estimators according to their ProxMSE is equivalent to that according to their MSE.

Proof. The proof follows directly from Lemma 2 in [14] (Appendix B.1). Namely, for any estimator we can write

$$\mathbb{E}[\|X - \hat{X}\|^2] = \mathbb{E}[\|(X - X^*) - (\hat{X} - X^*)\|^2] \quad (11)$$

$$= \mathbb{E}[\|X - X^*\|^2] + \mathbb{E}[\|\hat{X} - X^*\|^2] - 2\mathbb{E}[(X - X^*)^\top (\hat{X} - X^*)]. \quad (12)$$

Method	LFW-Test				WebPhoto-Test				WIDER-Test			
	FID ↓	Proxy MSE ↓	Proxy LPIPS ↓	Proxy CMSE ↓	FID ↓	Proxy MSE ↓	Proxy LPIPS ↓	Proxy CMSE ↓	FID ↓	Proxy MSE ↓	Proxy LPIPS ↓	Proxy CMSE ↓
VQFR [16]	51.31	126.8	0.221	46.8	75.86	156.7	0.278	45.8	44.09	282.6	0.333	41.0
CodeFormer [75]	52.84	90.1	0.205	38.7	83.93	78.7	0.250	33.6	39.22	141.3	0.274	31.5
GFPGAN [61]	50.32	110.7	0.223	64.9	87.29	626.9	0.316	532.1	39.29	296.1	0.319	137.0
RF++ [66]	50.72	89.1	0.211	26.0	75.50	334.3	0.282	247.3	45.45	201.3	0.317	29.8
DiffBIR [31]	40.90	82.8	0.283	18.5	92.67	82.9	0.357	16.9	35.83	120.0	0.345	18.6
PMRF [46]	49.49	40.1	0.251	13.5	81.03	41.9	0.308	12.9	41.19	86.3	0.328	16.1

Table 2. Quantitative comparison of leading end-to-end methods on real-world blind face restoration datasets. We evaluate perceptual quality via FID, distortion via ProxMSE, and ProxLPIPS, and consistency via ProxCMSE. We highlight the first, second, and third best-performing methods in each measure. PMRF stands out in ProxMSE and ProxCMSE, which comes with no surprise as the method is trained to achieve the best MSE possible under a perfect perceptual index constraint. In terms of perceptual quality alone, DiffBIR and RestorFormer++ generally outperforms the other methods.

By the law of total expectation, it follows that

$$\mathbb{E}[(X - X^*)^\top (\hat{X} - X^*)] = \mathbb{E} \left[\mathbb{E} \left[(X - X^*)^\top (\hat{X} - X^*) | Y \right] \right]. \quad (13)$$

Since \hat{X} and X are independent given Y , and since X^* is a function of Y , we have

$$\mathbb{E}[(X - X^*)^\top (\hat{X} - X^*)] = \mathbb{E} \left[\mathbb{E} \left[(X - X^*)^\top | Y \right] \mathbb{E} \left[(\hat{X} - X^*) | Y \right] \right]. \quad (14)$$

Now, it holds that

$$\mathbb{E} \left[(X - X^*)^\top | Y \right] = \mathbb{E} [X | Y] - \mathbb{E} [X^* | Y] \quad (15)$$

$$= \mathbb{E} [X | Y] - \mathbb{E} [X | Y] = 0. \quad (16)$$

Plugging this back to Eq. (14), we get $\mathbb{E}[(X - X^*)^\top (\hat{X} - X^*)] = 0$, and therefore Eq. (12) becomes

$$\text{MSE}(X, \hat{X}) = \mathbb{E}[\|X - \hat{X}\|_2^2] \quad (17)$$

$$= \mathbb{E}[\|X - X^*\|_2^2] + \mathbb{E}[\|\hat{X} - X^*\|_2^2] \quad (18)$$

$$= d^* + \mathbb{E}[\|\hat{X} - X^*\|_2^2] \quad (19)$$

where $d^* = \mathbb{E}[\|X - X^*\|_2^2]$ (the MSE of the MMSE estimator) does not change with \hat{X} , and

$$\mathbb{E}[\|\hat{X} - X^*\|_2^2] = \text{ProxMSE}(\hat{X}). \quad (20)$$

Subtracting d^* from both sides in Eq. (19) leads to the desired result. \square

C. MMSE estimator approximation effect

In practice, we only have an approximation of the true MMSE estimator X^* (e.g., a neural network trained to minimize the MSE loss). Denoting by \tilde{X}^* such an approximation of X^* , we are interested in the effect of the approximation error $R = \tilde{X}^* - X^*$ on the proposed ProxMSE measure. To this end, we present the following bound on the absolute error of ProxMSE.

Proposition 2. *The absolute error of ProxMSE when using \tilde{X}^* instead of X^* is bounded by*

$$\left| \mathbb{E}[\|\hat{X} - X^*\|_2^2] - \mathbb{E}[\|\hat{X} - \tilde{X}^*\|_2^2] \right| \leq \mathbb{E}[\|R\|_2^2] + 4\|R\|_1, \quad (21)$$

where $R = \tilde{X}^* - X^*$ and we assume that image pixels are taking values in $[0, 1]$.

Proof. We start by decomposing $\|\hat{X} - X^*\|_2^2$ and $\|\hat{X} - \tilde{X}^*\|_2^2$. Since $X^* = \tilde{X}^* - R$, it holds that

$$\|\hat{X} - X^*\|_2^2 = \|\hat{X}\|_2^2 + \|X^*\|_2^2 - 2\langle \hat{X}, X^* \rangle \quad (22)$$

$$= \|\hat{X}\|_2^2 + \|\tilde{X}^*\|_2^2 + \|R\|_2^2 - 2\langle \tilde{X}^*, R \rangle - 2\langle \hat{X}, X^* \rangle \quad (23)$$

$$= \|\hat{X}\|_2^2 + \|\tilde{X}^*\|_2^2 + \|R\|_2^2 - 2\langle \tilde{X}^*, R \rangle - 2\langle \hat{X}, \tilde{X}^* \rangle + 2\langle \hat{X}, R \rangle, \quad (24)$$

where we expanded $\|X^*\|_2^2$ in Eq. (23) and $\langle \hat{X}, X^* \rangle$ in Eq. (24). Moreover, we have

$$\|\hat{X} - \tilde{X}^*\|_2^2 = \|\hat{X}\|_2^2 + \|\tilde{X}^*\|_2^2 - 2\langle \hat{X}, \tilde{X}^* \rangle. \quad (25)$$

Taking the absolute difference between the expected values in Eqs. (22) and (25), we get

$$\left| \mathbb{E}[\|\hat{X} - X^*\|_2^2] - \mathbb{E}[\|\hat{X} - \tilde{X}^*\|_2^2] \right| = \left| \mathbb{E}[\|R\|_2^2 + 2\langle \hat{X}, R \rangle - 2\langle \tilde{X}^*, R \rangle] \right| \quad (26)$$

$$\leq \mathbb{E}[\|R\|_2^2] + 2\left| \mathbb{E}[\langle \hat{X}, R \rangle] \right| + 2\left| \mathbb{E}[\langle \tilde{X}^*, R \rangle] \right|, \quad (27)$$

where Eq. (27) holds due to the triangle inequality. Moreover,

$$\left| \mathbb{E} \left[\|\hat{X} - X^*\|_2^2 \right] - \mathbb{E} \left[\|\hat{X} - \tilde{X}^*\|_2^2 \right] \right| \leq \mathbb{E} [\|R\|_2^2] + 2\mathbb{E} \left[\left| \langle \hat{X}, R \rangle \right| \right] + 2\mathbb{E} \left[\left| \langle \tilde{X}^*, R \rangle \right| \right], \quad (28)$$

where we used Jensen’s inequality on the convex function $f(x) = |x|$.

Now, let us focus on $\left| \langle \hat{X}, R \rangle \right|$. By applying the triangle inequality and assuming that each entry in \hat{X} takes values in $[0, k]$, we get

$$\left| \langle \hat{X}, R \rangle \right| = \left| \sum_i \hat{X}_i R_i \right| \leq \sum_i \left| \hat{X}_i R_i \right| \leq \sum_i k |R_i| = k \|R\|_1. \quad (29)$$

Similarly, we have $\left| \langle \tilde{X}^*, R \rangle \right| \leq k \|R\|_1$. Substituting these bounds back into Eq. (28) and assuming $k = 1$ (as typically used in practice), we get

$$\left| \mathbb{E} \left[\|\hat{X} - X^*\|_2^2 \right] - \mathbb{E} \left[\|\hat{X} - \tilde{X}^*\|_2^2 \right] \right| \leq \mathbb{E} [\|R\|_2^2] + 4k\mathbb{E} [\|R\|_1] = \mathbb{E} [\|R\|_2^2] + 4\mathbb{E} [\|R\|_1] \quad (30)$$

□

In practice, computing R is impossible since X^* is unavailable. Hence, we showcase in controlled experiments (Section 4.3) that using an approximation of \tilde{X}^* still yields rankings that are consistent with the true MSE.

D. LPIPS is MSE in latent space

Denote by $f_l \in \mathbb{R}^{H_l \times W_l \times C_l}$ the channel-wise normalized feature of x from the l ’th layer and by $w_l \in \mathbb{R}^{C_l}$ a per-channel weight vector. To compute LPIPS [73], we average spatially and sum channel-wise a weighted ℓ_2 distance per element,

$$\Delta_{\text{LPIPS}}(x, \hat{x}) = \sum_l \frac{1}{H_l W_l} \sum_{h,w} \|w_l \odot (f_{h,w}^l - \hat{f}_{h,w}^l)\|_2^2. \quad (31)$$

This is equivalent to an MSE between flattened feature vectors. Denote by $z = [\text{vec}(z_1), \dots, \text{vec}(z_L)]^\top$, where $z_l = \frac{1}{\sqrt{H_l W_l}} w_l \odot f_l$, then

$$\Delta_{\text{LPIPS}}(x, \hat{x}) = \|z - \hat{z}\|_2^2 = \Delta_{\text{SE}}(z, \hat{z}). \quad (32)$$

E. Implementation details

E.1. Degradation estimator

Our degradation estimator consists of a ConvNext-Large [34] for feature extraction, two convolutional layers to sub-sample the extracted features, followed by an MLP head to transform the feature into four parameter values. The ConvNext is initialized from a robust ImageNet [11] checkpoint [32]. The architecture is illustrated in Fig. 12. We train the estimator on the FFHQ dataset [26] at 512×512 resolution for 300K steps and batch size 16 using the AdamW [35] optimizer ($\beta_1=0.9$, $\beta_2=0.999$, $\epsilon=10^{-8}$) with a constant learning rate of 2.5×10^{-5} , weight decay of 0.05, linear warmup for 1K steps, and linear cooldown for 20% steps [18] (for a total of 360K steps).

E.2. ELAD

We detail in Algorithm 2 *Empirical Likelihood Approximation with Diffusion prior (ELAD)*. We start with a concise summary of diffusion model notations used in the algorithm, based on DDIM [54], followed by the design choices taken in ELAD.

Notations. Denote the probability density function of clean images by $q(x_0)$. We construct a forward noising process as a Markov chain,

$$q(x_t|x_{t-1}) = \mathcal{N}(\sqrt{1 - \beta_t}x_{t-1}, \beta_t \mathbf{I}), \quad (33)$$

Method	CelebA-Test (Uniform Dist. #1)						CelebA-Test (Uniform Dist. #2)					
	MSE ↓	Proxy MSE ↓	LPIPS ↓	Proxy LPIPS ↓	CMSE ↓	Proxy CMSE ↓	MSE ↓	Proxy MSE ↓	LPIPS ↓	Proxy LPIPS ↓	CMSE ↓	Proxy CMSE ↓
VQFR [16]	277.2	164.2	0.35	0.226	–	48.1	637.4	364.7	0.45	0.355	46.31	50.5
CodeFormer [75]	217.0	103.8	0.34	0.209	–	41.7	429.7	151.1	0.40	0.245	54.38	59.9
GFPGAN [61]	245.5	129.5	0.36	0.232	–	67.8	636.9	363.6	0.47	0.369	117.30	122.4
RF++ [66]	213.3	102.6	0.34	0.217	–	30.4	554.2	282.0	0.45	0.354	30.14	35.2
DiffBIR [31]	209.4	99.0	0.39	0.297	–	26.2	384.1	100.2	0.44	0.326	27.66	35.3
<i>Plug & play</i>												
PGDiff [67]	341.6	227.3	0.40	0.313	–	84.2	712.4	441.5	0.47	0.379	93.00	93.5
DifFace [69]	229.6	114.9	0.40	0.306	–	63.6	371.7	90.9	0.44	0.308	50.83	58.0
ELAD (Ours)	215.1	100.8	0.39	0.296	–	52.1	363.7	83.4	0.43	0.306	42.41	49.2

Method	CelebA-Test (LFW Dist.)						CelebA-Test (WebPhoto Dist.)					
	MSE ↓	Proxy MSE ↓	LPIPS ↓	Proxy LPIPS ↓	CMSE ↓	Proxy CMSE ↓	MSE ↓	Proxy MSE ↓	LPIPS ↓	Proxy LPIPS ↓	CMSE ↓	Proxy CMSE ↓
VQFR [16]	199.0	128.8	0.32	0.210	40.33	44.5	239.3	147.6	0.34	0.218	37.22	39.2
CodeFormer [75]	158.9	88.9	0.32	0.199	31.58	35.0	188.1	97.0	0.33	0.204	27.37	29.7
GFPGAN [61]	176.7	107.7	0.33	0.210	54.93	59.0	214.9	123.2	0.35	0.222	55.33	57.6
RF++ [66]	163.3	93.3	0.31	0.200	22.19	26.7	187.1	97.0	0.33	0.208	19.34	21.6
DiffBIR [31]	157.0	88.1	0.35	0.277	10.48	14.6	184.4	94.8	0.37	0.287	10.65	12.8
<i>Plug & play</i>												
PGDiff [67]	276.4	204.4	0.38	0.309	92.39	95.8	314.3	220.8	0.39	0.312	77.37	79.1
DifFace [69]	208.8	134.3	0.39	0.312	71.35	73.9	219.0	124.4	0.39	0.309	56.50	58.2
ELAD (Ours)	191.4	117.3	0.38	0.299	56.91	59.6	202.8	108.6	0.39	0.298	44.23	45.9

Method	CelebA-Test (WIDER Dist.)					
	MSE ↓	Proxy MSE ↓	LPIPS ↓	Proxy LPIPS ↓	CMSE ↓	Proxy CMSE ↓
VQFR [16]	302.1	176.1	0.36	0.231	27.40	28.7
CodeFormer [75]	237.7	110.3	0.35	0.213	19.08	20.5
GFPGAN [61]	281.5	152.6	0.37	0.242	53.47	54.7
RF++ [66]	232.1	108.7	0.35	0.224	10.21	11.6
DiffBIR [31]	225.3	102.1	0.39	0.303	4.77	6.2
<i>Plug & play</i>						
PGDiff [67]	372.5	245.0	0.41	0.325	51.30	52.1
DifFace [69]	237.3	109.2	0.40	0.306	33.10	34.2
ELAD (Ours)	224.7	96.8	0.40	0.298	23.91	25.0

Table 3. Quantitative comparison between BFR methods on synthetic datasets defined in Section 3.2. We highlight the first, second, and third best-performing methods in each measure. We divide between end-to-end methods and plug-and-play ones. “Uniform Dist. #1” is used in Figure 7, while “Uniform Dist. #2” is used in Figure 4. “Uniform Dist. #1” is the dataset introduced in [61], which does not contain the degradations used, hence we cannot compute CMSE values.

where $t \in [1, \dots, T]$ is a timestep and $\{\beta\}_{t=1}^T$ is a noise scheduler and $q(x_T) \approx \mathcal{N}(0, \mathbf{I})$. We can sample from $q(x_t|x_0)$ directly by noting that

$$q(x_t|x_0) = \mathcal{N}(\sqrt{1 - \bar{\alpha}_t}x_0, (1 - \bar{\alpha}_t)\mathbf{I}), \quad (34)$$

where $\bar{\alpha}_t = \prod_{s=1}^t \alpha_s$ and $\alpha_t = (1 - \beta_t)$. Under DDIM, the task of a diffusion model is to construct a reverse denoising process by learning the following densities:

$$p_\theta(x_{t-1}|x_t) = \mathcal{N}\left(\sqrt{\bar{\alpha}_{t-1}}\hat{x}_0^t + \sqrt{1 - \bar{\alpha}_{t-1} - \sigma_t^2}\varepsilon_\theta(x_t, t), \sigma_t^2 \mathbf{I}\right), \quad (35)$$

where $\varepsilon_\theta(x_t, t)$ is a time-aware MMSE denoiser, $\hat{x}_0^t = (x_t - \sqrt{1 - \bar{\alpha}_t}\varepsilon_\theta(x_t, t))/\bar{\alpha}_t$, and $\sigma_t = \eta\beta_t \frac{1 - \bar{\alpha}_{t-1}}{1 - \bar{\alpha}_t}$. Using $\eta \in [0, 1]$, we can control the amount of random noise injected in each step. Choosing $\eta = 0$ results in a deterministic sampler, while $\eta = 1$ leads to the DDPM [21] sampler.

Algorithm design. Following DPS [8], we guide the diffusion process by taking steps in the direction of the score-likelihood $p(x_t|y)$ at time t . Similar to prior work [8, 55, 76], we approximate $p(x_t|y) \approx p(\hat{x}_0^t|y)$ and compute $p(\hat{x}_0^t|y)$ using ELA based on the estimated degradation $a_\theta(y)$. Like DiffFace [69], we perform 100 denoising steps, starting from an intermediate timestep ($T_0 = 400$ out of $T = 1,000$ steps) initialized by an MMSE restoration of y for accelerated sampling. We use a DDIM [54] sampler with $\eta = 0.5$, where we recompute the predicted noise after each score-likelihood step, similar to DiffPIR [76] for increased stability. We adapt the diffusion prior trained by DiffFace [69]. Still, we emphasize that our method does not depend on a specific diffusion prior, and the results could be improved by utilizing better priors.

As we approximate $p(x_t|y) \approx p(\hat{x}_0^t|y)$, we employ a dynamic step size. We achieve good performance using a step size equal to the ratio between the current signal-to-noise ratio (SNR) and the SNR at the initial timestep, multiplied by a constant λ ($=10^{-2}$ in practice). Moreover, similar to the classifier (free) guidance literature [50], we find that clipping the score likelihood further stabilizes the process.

To approximate the mean $\mu(\hat{x}_0^t, a_\theta(y))$ we compute an empirical sample mean by sampling 16 samples from $p_{Y|X,A}(\cdot|X = \hat{x}_0^t, A = a_\theta(y))$ each denoising step. Moreover, instead of assuming isotropic likelihood, we approximate the standard deviation empirically using the same samples, resulting in a diagonal covariance.

Algorithm 2: ELAD - Blind Restoration Diffusion Sampler. Full version of Algorithm 1

Data: measurement y , degradation estimator a_θ , MMSE regressor f , diffusion noise predictor ε_θ , diffusion schedule $\{\bar{\alpha}_t\}_{t=1}^T$, start time $T_0 \leq T$, DDIM coefficient η , ELA coefficient λ

Result: a restored image x_0

```

1  $x_{T_0} \sim \mathcal{N}(\sqrt{1 - \bar{\alpha}_{T_0}}f(y), (1 - \bar{\alpha}_{T_0})\mathbf{I})$  // noise MMSE restoration to step  $T_0$ 
2  $\hat{a} = a_\theta(y)$  // predict degradation
3 for  $t = T_0$  to 1 do
4    $\hat{x}_0^t = (x_t - \sqrt{1 - \bar{\alpha}_t}\varepsilon_\theta(x_t, t))/\bar{\alpha}_t$  // perform denoising step
5    $\lambda_t = \frac{1}{\bar{\alpha}_{t-1}} \frac{\text{SNR}_t}{\text{SNR}_{T_0}} \lambda$  // compute dynamic step size
6    $g = \nabla_{\hat{x}_t} \|y - \mu(\hat{x}_0^t, \hat{a})\|_2^2$  // compute score likelihood
7    $\hat{x}_0^t = \hat{x}_0^t - \lambda_t \cdot g.\text{clamp}(-1, 1)$  // perform likelihood step
8    $\hat{\varepsilon} = \frac{1}{\sqrt{1 - \bar{\alpha}_t}}(x_t - \sqrt{\bar{\alpha}_t}\hat{x}_0^t)$  // compute effective noise
9    $x_{t-1} = \text{DDIMStep}(\hat{x}_0^t, \hat{\varepsilon}, \eta)$  // perform DDIM step
10 end

```

F. Datasets analysis & synthesis

F.1. Real-world datasets analysis

Prior work [75] considered the degradations in LFW simpler than those in WebPhoto and WIDER. However, they could not justify those claims quantitatively as the degradations in those datasets are unknown. Using our degradation estimator, we presented in Figure 3 the estimated distribution of degradation parameters in BFR real-world datasets. The estimation confirms that images in the LFW dataset have undergone blur and downsampling operations sampled from a narrower distribution centered on lower values than WebPhoto and WIDER distributions, leading to a simpler restoration task. Yet, we also reveal that LFW images were compressed more aggressively compared to other datasets, an observation that might not have been easily made before.

F.2. Synthetic datasets examples

Throughout the paper we use the real datasets LFW-Test, WebPhotos-Test, and WIDER-Test to the proposed tools. In Sec. 3.2 we additionally demonstrate how we can leverage the degradation estimator to analyze those datasets.

To demonstrate the effectiveness of our degradation estimator, we present in Figure 13 examples of degraded images from each dataset, and we predict the degradation of each. Using each predicted degradation we synthesize a synthetic degraded image from a clean CelebA-Test image.

As described in Sec. 3.2, we approximate the distribution of A for each dataset by predicting the degradations of each image using our estimator and fitting a KDE over the predictions. In Appendix F.2 we present examples from the synthetic datasets alongside images from the real datasets. Note that in this figures the image are not paired, as each degraded image is created by sampling randomly from the estimated distribution of A .

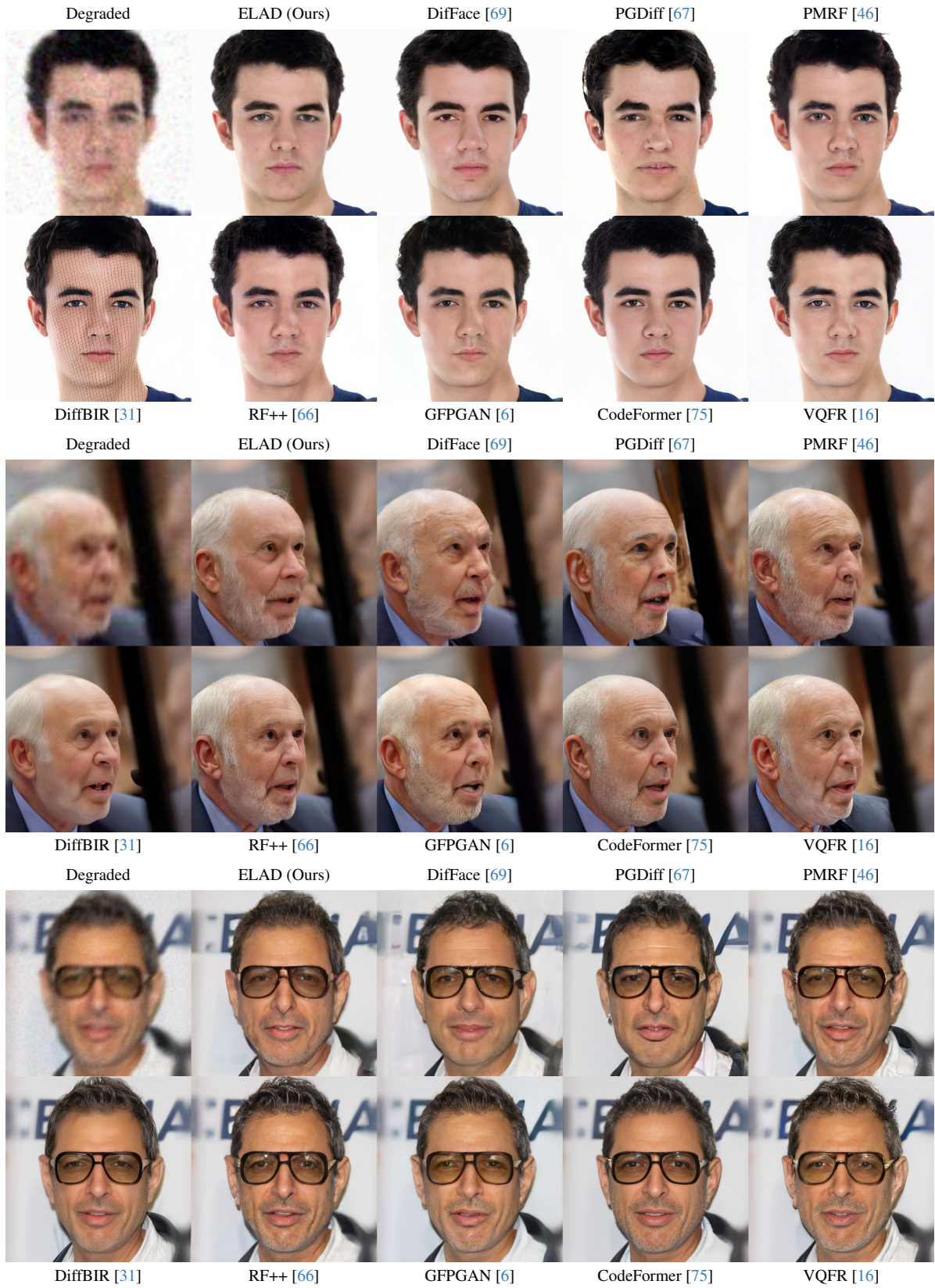


Figure 8. Restoration examples on CelebA-Test [61].



Figure 9. Restoration examples on LFW-Test [22].

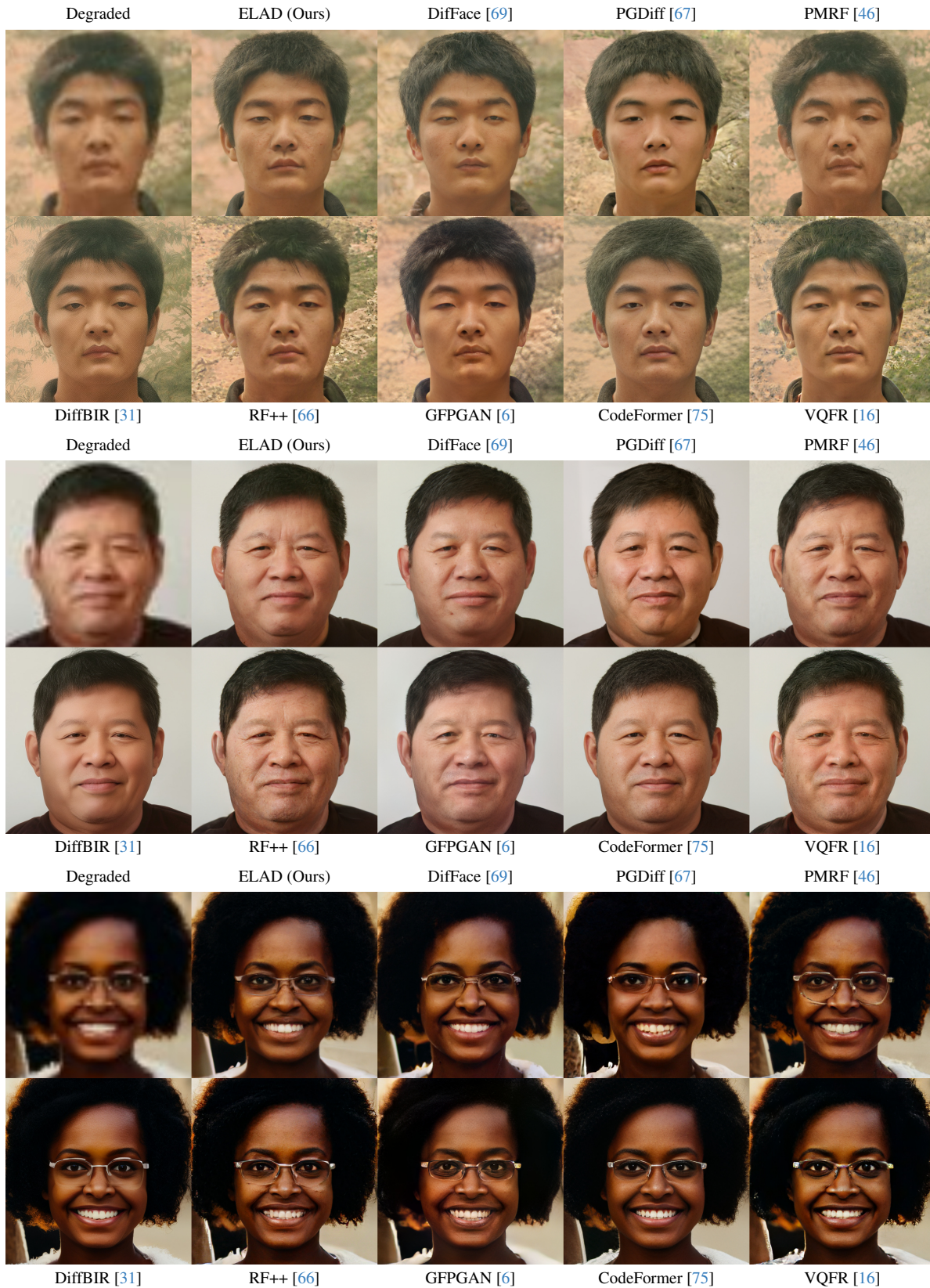


Figure 10. Restoration examples on WebPhot-Test [61].

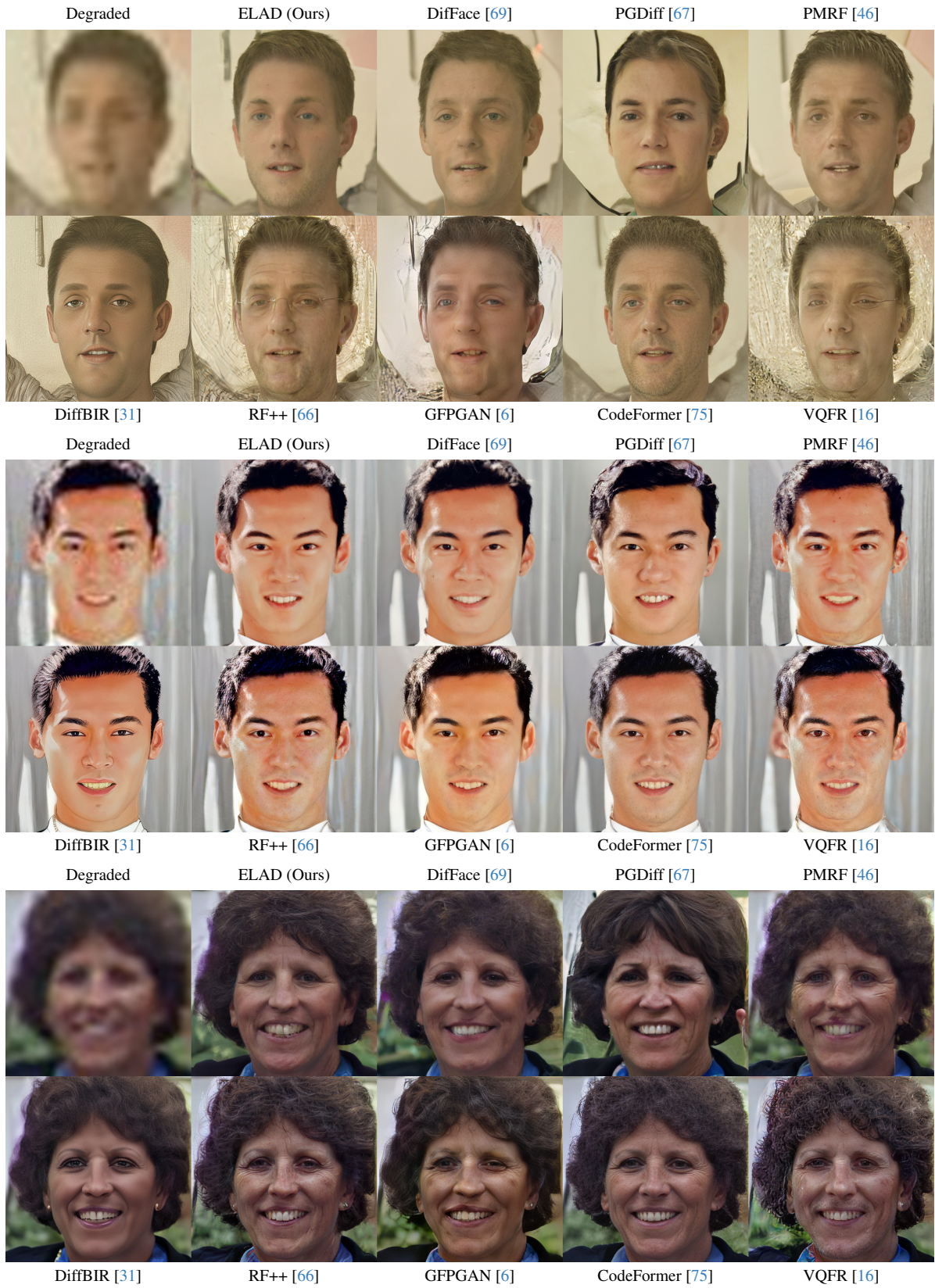


Figure 11. Restoration examples on WIDER-Test [68].

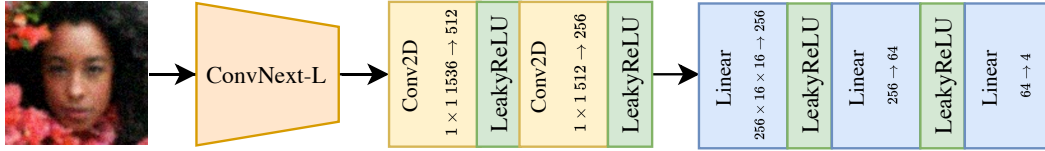


Figure 12. Degradation estimator architecture for BFR.

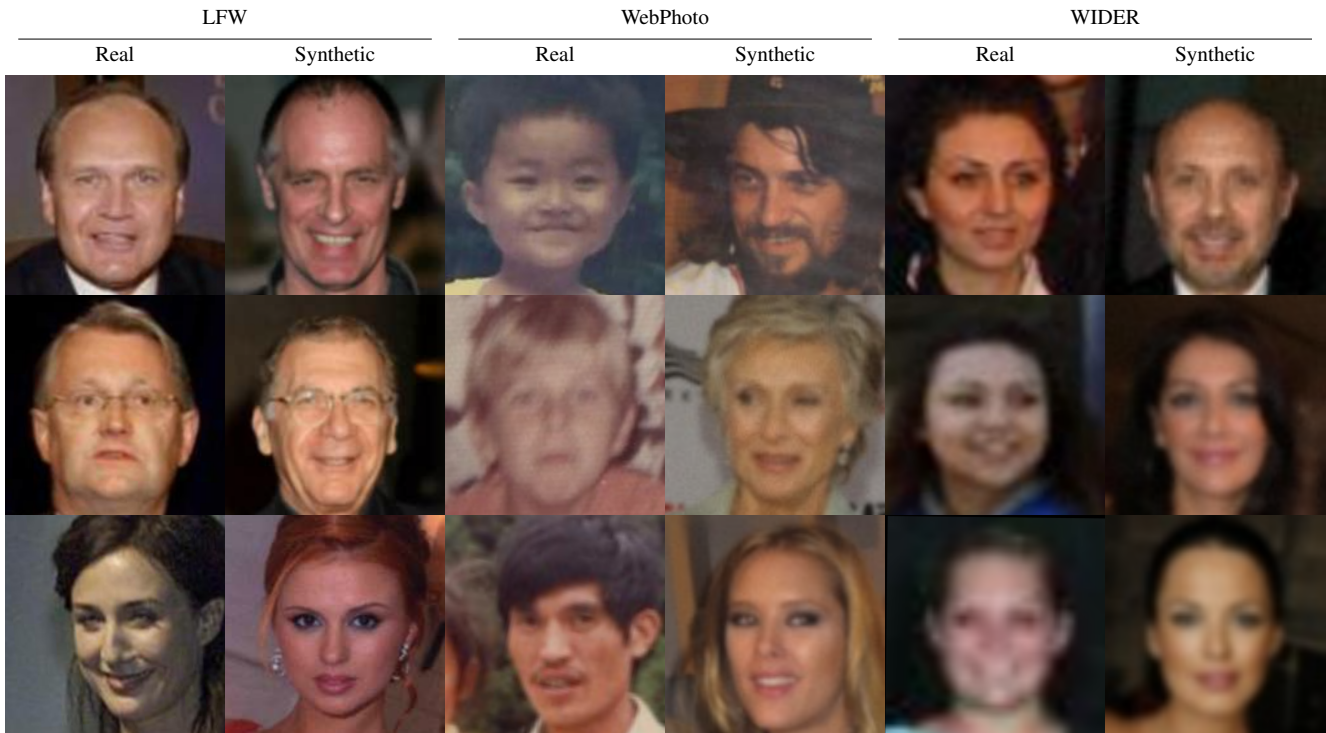


Figure 13. Images from real datasets paired with images from CelebA synthetically degraded by the predicted degradation.

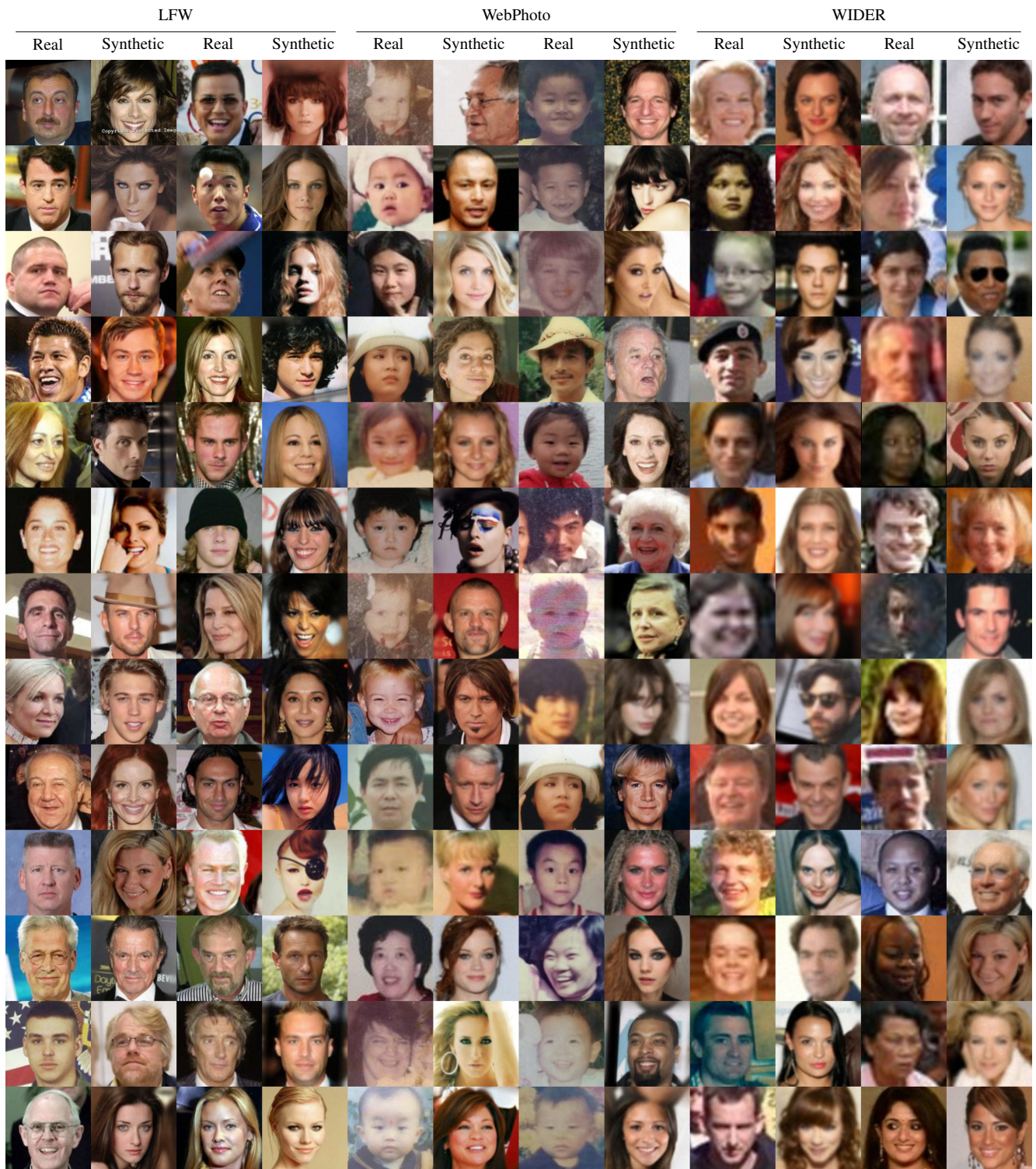


Figure 14. More samples of real and synthetic images. The real images come from the LFW-Test, WebPhoto-Test, and WIDER-Test datasets. The synthetic images mimic those datasets as explained in Figure 13.